Draft version February 5, 2008
Preprint typeset using LaTeX style emulateapj v. 6/22/04

THE LOW-z INTERGALACTIC MEDIUM. II. Lyβ, O VI, AND C III FOREST

Charles W. Danforth, J. Michael Shull, Jessica L. Rosenberg[1], & John T. Stocke
Center for Astrophysics and Space Astronomy, Dept. of Astrophysial & Planetary Sciences, University of Colorado, Boulder, CO 80309;
danforth@casa.colorado.edu, mshull@casa.colorado.edu, stocke@casa.colorado.edu

Draft version February 5, 2008

ABSTRACT

We present the results of a large survey of H I, O VI, and C III absorption lines in the low-redshift ($z < 0.3$) intergalactic medium (IGM). We begin with 171 strong Lyα absorption lines ($W_\lambda \geq 80$ mÅ) in 31 AGN sight lines studied with the *Hubble Space Telescope* and measure corresponding absorption from higher-order Lyman lines with *FUSE*. Higher-order Lyman lines are used to determine $N_{\rm HI}$ and $b_{\rm HI}$ accurately through a curve-of-growth (COG) analysis. We find that the number of H I absorbers per column density bin is a power-law distribution, $d\mathcal{N}/dN_{\rm HI} \propto N_{\rm HI}^{-\beta}$, with $\beta_{\rm HI} = 1.68 \pm 0.11$. We made 40 detections of O VI $\lambda\lambda$1032,1038 and 30 detections of C III λ977 out of 129 and 148 potential absorbers, respectively. The column density distribution of C III absorbers has $\beta_{\rm CIII} = 1.68 \pm 0.04$, similar to $\beta_{\rm HI}$ but not as steep as $\beta_{\rm OVI} = 2.1 \pm 0.1$. From the absorption-line frequency, $d\mathcal{N}_{\rm CIII}/dz = 12^{+3}_{-2}$ for $W_\lambda({\rm CIII}) > 30$ mÅ, we calculate a typical IGM absorber size $r_0 \sim 400$ kpc, similar to scales derived by other means. The COG-derived b-values show that H I samples material with $T < 10^5$ K, incompatible with a hot IGM phase. By calculating a grid of CLOUDY models of IGM absorbers with a range of collisional and photoionization parameters, we find it difficult to simultaneously account for the O VI and C III observations with a single phase. Instead, the observations require a multiphase IGM in which H I and C III arise in photoionized regions, while O VI is produced primarily through shocks. From the multiphase ratio $N_{\rm HI}/N_{\rm CIII}$, we infer the IGM metallicity to be $Z_C = 0.12\,Z_\odot$, similar to our previous estimate of $Z_O = 0.09\,Z_\odot$ from O VI.

Subject headings: cosmological parameters—cosmology: observations—intergalactic medium—quasars: absorption lines

1. INTRODUCTION

The study of the intergalactic medium (IGM) is crucial for understanding the structure and evolution of galaxies. Much has been learned from the distribution of visible galaxies in large-scale structure, but a large fraction of the baryonic mass of the universe still resides in the IGM (Cen & Ostriker 1999a; Cen et al. 2001; Davé et al. 1999, 2001), even at low redshift (Stocke, Shull, & Penton 2005). These intergalactic absorbers are likely composed of primordial material left over from the big bang and processed material ejected from galaxies. The identification of these absorbers and their origins will help to constrain both the evolution of primordial gas in the universe as well as galactic outflows and metal processing. By comparing local, low-redshift IGM absorbers with those in the high-redshift universe, we can watch the evolution of these processes through cosmic time.

The IGM is best probed with absorption-line studies using distant continuum sources such as quasars and AGN. H I is best detected through Lyman line absorption in the rest-frame far ultraviolet (FUV; 912–1216 Å), particularly Lyα at 1216 Å. Ironically, much analysis has been done of the Lyα forest and metal lines in the distant universe ($2 < z < 5$), but comparatively little exists for the local universe ($z < 1$). To fill this gap in our knowledge, we must examine the IGM in the FUV.

The Lyα line is arguably the most important diagnostic of the IGM, but it has inherent limitations. Strong lines exhibit saturation and blending from weaker, unresolved components. Profile fits to the Lyα line tend to underestimate H I column density and overestimate the Doppler width (Shull et al. 2000). For more accurate analysis, weaker Lyman lines such as Lyβ are required in conjunction with Lyα. The trade-off is that weaker lines are more difficult to detect and, at low redshift, lie in a wavelength range complicated with H_2 and ionic lines from the local interstellar medium (ISM).

The *Hubble Space Telescope* (HST) has housed a pair of ultraviolet instruments, the *Goddard High Resolution Spectrograph* (GHRS) and the *Space Telescope Imaging Spectrograph* (STIS), which have brought UV spectroscopy into a golden age with high-resolution spectrographic capabilities down to ∼1150 Å. The *Far Ultraviolet Spectroscopic Explorer* (*FUSE*) complements the capabilities of HST, providing coverage of the 905–1187 Å band with the higher Lyman lines missed by HST at $z < 0.12$ as well as the important diagnostic lines of O VI $\lambda\lambda 1032, 1038$ and C III λ977 out to modest redshifts (Moos et al. 2000).

These spectrographs have compiled a sizeable catalog of IGM absorbers along extragalactic sight lines. Absorption systems in the IGM can be identified using strong Lyα lines in the relatively uncomplicated spectral region of GHRS and STIS data. Once located, the higher Lyman lines and metal diagnostics covered by *FUSE* give a much more complete picture of the system.

In this study, we use published catalogs of Lyα absorbers in extragalactic sight lines and search for coun-

[1] NSF Astronomy and Astrophysics Postdoctoral Fellow, currently at Harvard-Smithsonian Center for Astrophysics; jlrosenberg@cfa.harvard.edu

terpart absorption in the higher Lyman lines (Lyβ, Lyγ, Lyδ, etc) to more accurately determine the column density $N_{\rm HI}$ and Doppler line width $b_{\rm HI}$ for neutral hydrogen in the IGM. Furthermore, we look for counterpart absorption in probes of the crucial warm-hot ionized medium (WHIM), O VI $\lambda\lambda$1031.926, 1037.617 and possibly C III λ977.020. O VI is present in gas at 10^{5-6} K and is thought to arise from shock ionization perhaps with some contribution from hard, ionizing external radiation in low density gas. The H I absorption can be seen in the *FUSE* band at $0.003 < z < 0.3$, while O VI and C III can be measured between $0 < z < 0.15$ and $0 < z < 0.21$, respectively. We use these lines to gain better understanding of how gas becomes ionized in the low-redshift universe.

We gave an overview of the project and some of the more important cosmological results in Danforth & Shull (2005; henceforth Paper I). In this paper, we describe in complete detail our catalog of 171 Lyα absorbers in sight lines toward 31 AGN, including several dozen new Lyα absorbers. We also describe our survey of Lyβ and C III absorbers. We present our criteria for selection of sight lines and absorber in § 2 along with a list of previously unpublished Lyα absorbers. Our analysis methods and results are presented in § 3. In § 4 we discuss the importance of multiple Lyman lines to accurate H I measurements, analyze the distribution of C III detections, discuss new evidence for a multiphase IGM, and investigate the metallicity of the IGM. We summarize our conclusions in § 5.

2. SIGHT LINES AND ABSORBERS

The catalog of *FUSE* observations of extragalactic sight lines is large enough that a statistical study of O VI in the low-redshift IGM is feasible. We searched the catalog of observations for sight lines with previous quasar absorption-line studies. The majority of our target list was obtained from the Colorado surveys based on GHRS and STIS grating observations of 30 AGN (Penton, Stocke, & Shull 2000; Penton, Shull, & Stocke 2000; Penton, Stocke, & Shull 2003, 2004). Six of these targets lack *FUSE* data of sufficient quality to be included in our survey. The target list was augmented by additional studies of these sight lines from the literature, using all available moderate and high-resolution UV data. We analyzed archival STIS/E140M echelle data for six additional sight lines as described below. Our final sample consists of 31 sight lines with reasonable quality *FUSE* data and a known set of Lyα absorbers (or a known lack of Lyα absorbers) over at least part of their path length (Table 1). The total pathlength surveyed for Lyα absorbers is noted in column 7 of Table 1.

One of our goals was to rigorously determine the H I column density for the IGM absorbers via curves of growth. Different authors use different techniques to determine column densities and b-values, resulting in a heterogenous sample of absorber information. For this reason, the primary information we take from the Lyα surveys is absorber redshift $z_{\rm abs}$ and Lyα equivalent width $W_{\rm Ly\alpha}$, both of which are measured directly from the data and are not subject to analytical interpretation.

In six cases, we used archival STIS/E140M data and performed our own Lyα absorber search. The data were smoothed by three pixels to better match the instrumental resolution. For four targets (PKS 0405−123, PG 0953+415, PG 1259+593, and PKS 1302−102), our analysis was carried out as follows: (1) the major absorption and emission line regions were marked by hand for exclusion; (2) the excluded regions of the spectrum were then replaced with a linear interpolation over ten pixels on either side of the excluded region; (3) a rough smoothing over 100 pixels was applied to the resulting continuum;, finally (4) a cubic-spline linear interpolation was derived from all of the continuum data points that were less than 2σ from the smoothed continuum value. This linear interpolation over points deviating by less than 2σ from the smoothed value for the continuum was the fit used in the processing of the data. The one exception was for lines that fell on the damping wings of Galactic Lyα; in these cases a local fit to the continuum was performed.

The measurement of the absorption lines in the E140M data was performed using the program VPFIT[2] which performs Voigt profile fitting for each of the lines. The line fitting was performed interactively for each of the lines. In general, we were conservative about adding multiple components to the fit since the fit can almost always be improved by adding these components even if it is not justified by an F-test. We did, however, add multiple components to the Lyα fits in cases where the higher Lyman lines or metal lines for the same absorber indicated a multi-component structure. In some of these cases, we use the information derived from the high-order lines to fix the positions and/or the b-values for the Lyα line fits.

In two other cases, HE 0226−4110 and PHL 1811, we analyzed the STIS/E140M data using an IDL code in a manner procedurally similar to that described above. Strong absorption lines at $\lambda > 1216$ Å were flagged as possible intervening Lyα lines. Candidate Lyα lines were confirmed by checking for counterpart Lyβ and Lyγ absorption before being accepted. Equivalent widths were measured interactively from the normalized Lyα profiles. As above, multiple components were not used unless there was compelling evidence for their existence in weaker Lyman lines. The STIS/G140M data for Mrk 876 were analyzed similarly. In all, our analysis yielded consistent results with published data in terms of velocities and equivalent widths.

The distribution of H I absorbers as a function of column density is a power law with a negative slope as discussed below (Penton, Shull, & Stocke 2000; Penton, Stocke, & Shull 2004). Thus, the absorber list features many weak absorbers and relatively few strong systems. The ratio of equivalent widths for unsaturated H I absorbers is equal to the ratio of $f\lambda^2$ between the lines, a factor of 6.24 for Lyα and Lyβ. Since the 3σ limiting equivalent width of good *FUSE* data is typically 10-20 mÅ, we set an equivalent width threshold of $W_{\rm Ly\alpha} > 80$ mÅ to have any realistic chance of detecting weaker Lyman series or ionic lines. Profile fits to weak Lyα lines typically give more accurate column densities than strong lines (in the absense of a sufficiently optically thin higher order line), so curve-of-growth (COG) fitting

[2] VPFIT was written by R. F. Carswell, J. K. Webb, M. J. Irwin, & A. J. Cooke. More information is available at `http://www.ast.cam.ac.uk/~rfc/vpfit.html`

TABLE 1
FUSE IGM Sight Lines

Target AGN	Alternate Name	RA (J2000) h m s	Dec (J2000) ° ′ ″	AGN type	$z_{\rm AGN}$	$\Delta z_{\rm Ly\alpha}$[a]	$\mathcal{N}_{\rm abs}$[b]	FUSE ID	Exp. (ksec)
Mrk 335	PG 0003+199	00 06 19.5	+20 12 10.3	Syf1	0.0256	0.0159	3	P10102	97.0
I Zw1	PG 0050+124	00 53 34.9	+12 41 36.0	Gal	0.0607	0.0298	3	P11101	38.6
Ton S180	HE 0054−2239	00 57 20.0	−22 22 59.3	Syf1.2	0.0620	0.0570	6	P10105	16.6
Fairall 9	···	01 23 46.0	−58 48 23.8	Syf1	0.0461	0.0378	1	P10106	38.9
HE 0226−4110	···	02 28 15.2	−40 57 16	QSO	0.495	0.4061	11	multiple[c]	33.2
NGC 985	Mrk 1048	02 34 37.8	−08 47 15.6	Syf1	0.0431	0.0381	0	P10109	68.0
PKS 0405−12	···	04 07 48.2	−12 11 31.5	QSO	0.574	0.4061	7	B08701	71.1
Akn 120	Mrk 1095	05 16 11.4	−00 08 59.4	Syf1	0.0331	0.0225	1	P10112	56.2
VII Zw118	···	07 07 13.1	+64 35 58.8	Syf1	0.0797	0.0266	1	multiple[c]	198.6
PG 0804+761	···	08 10 58.5	+76 02 41.9	QSO	0.1000	0.0686	2	multiple[c]	174.0
Ton 951	PG 0844+349	08 47 42.5	+34 45 03.5	QSO	0.064	0.0590	0	P10120	31.9
PG 0953+414	···	09 56 52.8	+41 15 25.7	QSO?	0.239	0.2340	15	P10122	72.1
Mrk 421	···	11 04 27.3	+38 12 32.0	Blazar	0.0300	0.0203	1	multiple[c]	83.9
PG 1116+215	Ton 1388	11 19 08.7	+21 19 18.2	QSO	0.1763	0.0686	11	P10131	77.0
PG 1211+143	···	12 14 17.6	+14 03 12.7	Syf	0.0809	0.0686	12	P10720	52.3
3C 273	PG 1226+023	12 29 06.7	+02 03 08.9	QSO	0.1583	0.1533	8	P10135	42.3
PG 1259+593	···	13 01 13.1	+59 02 05.7	QSO	0.472	0.4061	20	P10801	668.3
PKS 1302−102	PG 1302−102	13 05 32.8	−10 33 22.0	QSO	0.286	0.2810	18	P10802	142.7
Mrk 279	PG 1351+695	13 53 03.4	+69 18 29.9	Syf1	0.0306	0.0200	0	multiple[c]	228.5
Mrk 1383	PG 1426+015	14 29 06.6	+01 17 06.6	Syf1	0.0865	0.0686	2	multiple[c]	63.5
Mrk 817	PG 1434+590	14 36 22.1	+58 47 39.5	Syf1.5	0.0313	0.0206	1	P10804	189.9
Mrk 478	PG 1440+356	14 42 07.5	+35 26 22.9	Gal	0.0791	0.0686	3	P11109	14.2
Mrk 290	PG 1534+580	15 35 52.4	+57 54 09.3	Syf1	0.0296	0.0114	0	P10729	12.8
Mrk 876	PG 1613+658	16 13 57.2	+65 43 10	QSO	0.129	0.0266	2	P10731	46.0
H 1821+643	···	18 21 57.3	+64 20 36.3	Syf1	0.2968	0.2810	16	P10164	132.3
PKS 2005−489	···	20 09 25.4	−48 49 53.9	BLLac	0.0710	0.0660	4	multiple[c]	49.2
Mrk 509	···	20 44 09.7	−10 43 24.7	Syf1	0.0344	0.0263	1	P10806	62.3
II Zw136	PG 2130+099	21 32 27.8	+10 08 19.4	Syf1	0.0630	0.0580	1	P10183	22.7
PHL 1811	···	21 55 01.6	−09 22 26.0	Syf1	0.192	0.1870	14	multiple[c]	75.0
PKS 2155−304	···	21 58 52.1	−30 13 32.3	BLLac	0.1165	0.0585	8	P10807	123.2
MR 2251−178	···	22 54 05.8	−17 34 55.0	Gal	0.0644	0.0594	2	P11110	54.1

[a]Redshift pathlength Δz surveyed for Lyα absorption. We only use absorbers at $z < 0.3$ in this work.
[b]$\mathcal{N}_{\rm abs}$ is the number of Lyα absorbers $W_\lambda > 80$ mÅ at $z_{\rm abs} < 0.3$.
[c]Multiple FUSE observations are as follows: HE 0226−4110=P10191, P20713; VII Zw118=P10116, S60113; PG 0804+761=P10119, S60110; Mrk 421=P10129, Z01001; Mrk 279=P10803, C09002, D15401; Mrk 1383=P10148, P26701; PKS 2005−489=P10738, C14903; PHL 1811=P10810, P20711

from multiple transitions is less crucial.

We also limited the sample to those absorbers at $z \leq 0.3$ where the Lyman limit is still within the *FUSE* band. This limits our analysis to the "local", low-redshift universe. Furthermore, as in Penton, Stocke, & Shull (2000), any absorber within $cz = 1500$ km s^{-1} of the AGN emission velocity was discarded as being potentially related to the AGN. However, quasar outflow velocities have been measured at much higher velocities (Crenshaw et al. 1999; Kriss 2002) and absorbers within $\sim$5000 km s^{-1} of $v_{\rm AGN}$ were treated individually. Broad, asymetric line profiles, especially in metal lines, were used as a criterion in a few cases to disqualify absorbers as intrinsic to the AGN system (N. Arav and J. Gabel, priv comm.).

Our final census is 171 known H I absorbers with $z \leq 0.30$ and $W_{\rm Ly\alpha} > 80$ mÅ. Of these, there are 148 absorbers at $z \leq 0.21$, where C III λ977 absorption appears within the *FUSE* range, and 129 potential O VI λ1032 absorbers at $z \leq 0.15$. These absorbers, along with reference information, are listed in Table 2 and assigned identification numbers based on sight-line and redshift ordering. Four sight lines in Table 1 (NGC 985, Ton 951, Mrk 279, and Mrk 290) are devoid of strong Lyα absorbers ($W > 80$ mÅ) and not listed in Table 2. These sight lines were not analyzed for high Lyman series or metal absorption, but they contribute to the total redshift path length and are valid statistical contributors to the sample.

3. DATA ANALYSIS

Once the Lyα absorbers were established with reliable redshifts and equivalent widths (either from the literature or from our own analysis of the archival data), we analyzed the *FUSE* data for each absorber in up to six Lyman-series transitions: Lyβ λ1025.722, Lyγ λ972.537, Lyδ λ949.743, Lyϵ λ937.803, Lyζ λ930.748, and Lyη λ926.226. We also analyzed the metal transitions O VI λ1031.9261, O VI λ1037.6167, and C III λ977.0201.

Data were retrieved from the archive and reduced locally using CALFUSEv2.4[3]. Raw exposures within a single *FUSE* observation were coadded by channel midway through the pipeline. This can produce a significant improvement in data quality for faint sources (such as AGN) since the combined pixel file has higher S/N than the individual exposures and consequently the extraction apertures are more likely to be placed correctly. Combining exposures also speeds up reduction time dramatically. Reduced data were then shifted and coadded by observation to generate a final spectrum from each of the

[3] More detailed calibration information is available at `http://fuse.pha.jhu.edu/analysis/calfuse_intro.html`

eight data channels. The data were binned by three pixels; *FUSE* resolution is typically 8-10 pixels or roughly 3 bins.

The data were normalized in 10 Å segments centered on the location of each IGM absorber as follows: the locations of prominent Galactic ISM lines, IGM lines, and intrinsic absorption lines from the AGN were marked automatically. Line-free regions were then selected interactively and fitted using Legendre polynomials of order less than six. The signal to noise per binned pixel $(S/N)_{\rm pix}$ was established locally as the 1σ deviation from the mean in the line-free continuum regions within 5 Å of the IGM line. Given that a *FUSE* resolution element is typically 8–10 raw pixels ($\sim$3 binned pixels) or $\Delta V \approx 20$ km s^{-1}, we adopt the relationship $(S/N)_{\rm res} = \sqrt{3}\,(S/N)_{\rm pix}$ throughout this study. Absolute velocity calibration in *FUSE* data is not determined to much better than a resolution element. We calibrated each segment by setting Galactic H_2 lines to $v_{\rm lsr} = 0$. If H_2 lines were unavailable, low-ionization ISM lines (Ar I, Si II, Fe II, P II) in the area were used or, if necessary, other IGM lines. This process was carried out for each transition of each absorber in each of up to four detector channels covering the wavelength region.

Once a collection of normalized spectral segments was generated, the quantitative analysis began. Each transition was examined and measured interactively in two ways. A multi-component Voigt profile fit was performed on the IGM absorber as well as on any other nearby lines with free parameters, v, b, and $N_{\rm fit}$. From b and $N_{\rm fit}$, the equivalent width $W_{\rm fit}$ was determined. We used as few absorption components as possible in our fits since arbitrary additional components always improve the fit visually. Second, an apparent column density $N_{\rm a}$, line width, $W_{\rm a}$, and velocity centroid were determined via techniques described in Savage & Sembach (1991). Roughly half of the lines in our survey were fit using both apparent column and Voigt fitting techniques and the resulting column densities, velocity centroids, b-values, and equivalent widths are within the uncertainties in most cases for low or moderate-saturation lines. Voigt fitting tends to give more reliable results for saturated lines and lines where blending and multiple components are present. The apparent column method is superior in noisy data or in weak absorbers where a profile fit will be heavily influenced by noise. All equivalent widths were shifted to the rest frame: $W_{\rm r} = W_{\rm obs}(1+z)^{-1}$.

A 3σ upper limit on equivalent width was also determined for each absorber based on the spectrograph resolution $R = \lambda/\Delta\lambda$ and local signal-to-noise per resolution element $(S/N)_{\rm res}$,

$$W_{\rm min} = \frac{3\ \lambda}{R\ (S/N)_{\rm res}}, \qquad (1)$$

where $R = \lambda/\Delta\lambda \approx 15,000$. In cases where no absorption was detected or when a detection was below a 3σ level, the upper limit equivalent width was substituted. In cases where a line was strongly blended, the total, blended equivalent width was used as an upper limit.

Roughly half the sight lines featured moderate to strong absorption by Galactic H_2 at $\lambda < 1120$ Å out of rotational levels $J \leq 4$. We modeled and removed these lines when possible using a database of H_2 column measurements compiled by Gillmon et al. (2005). However, the modeled H_2 profiles were not always precise enough to leave a flat, residual-free continuum in unblended H_2 lines, so cases of H_2 contamination in IGM lines were treated with caution. When in doubt, the H_2 was not modeled, and the fit to the contaminated line was treated as an upper limit.

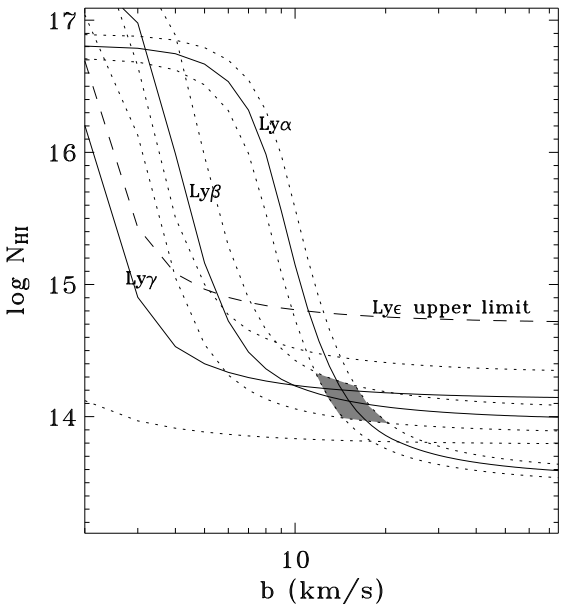

FIG. 1.— Concordance plot for the absorber at $z = 0.0071$ toward PKS 1211+143 used to determine an accurate values of $b_{\rm HI}$ and $N_{\rm HI}$. Any given equivalent width corresponds to a curve in b-N space. Multiple curves give accurate values for N and b. Dotted lines represent 1σ errors in measured W_λ and the dashed line shows the upper limit measurement of $W_{{\rm Ly}\epsilon}$. The Lyδ line for this absorber was blended with an H_2 line and was unavailable. The shaded area shows the derived b, N value and associated uncertainty.

Once all lines were measured, data from all four instrument channels were compared side-by-side. This allowed us to interactively reject spurious detections (features appearing in only one channel) and instrumental features, and to systematically verify the existence of weak absorbers. Of particular note is the strong instrumental "absorption feature" at 1043.5 Å in the LiF1a channel (see Sahnow et al. 2000, for an overview of the *FUSE* detectors and specifications). A surprising number of absorbers fell on or near this feature, and we were forced to use the lower-throughput LiF2b channel instead. Fitted quantities (or upper limits) from the channel with the best quality data were chosen as representative of the line. In the majority of cases, the LiF1 channel was used, but LiF2 was superior $\sim$ 30% of the time. The SiC channels have much lower throughput than the LiF channels and were only used for lines that fell outside the LiF coverage ($\lambda < 1000$ Å) or in the LiF chip gap (1084 Å $< \lambda <$ 1087 Å).

3.1. *H I Analysis*

Column densities and b-values for the H I absorbers were determined via COG concordance plots (see Shull et al. 2000), an example of which is shown in Fig-

ure 1. Each value of equivalent width for a particular set of atomic parameters traces out a curve in b, N space. By plotting curves from several transitions with a high contrast in $f\lambda$, we can determine the accurate column density $N_{\rm cog}$ and b-value. This method is equivalent to a traditional curve of growth fit, but it gives a better idea of the degree of uncertainty involved in both parameters. In several cases, anomalously strong absorption in one Lyman line or another was caught and corrected by this technique.

Several Lyα absorbers in our sample show clear evidence of multiple components, and many others undoubtedly feature unresolved structure. Since our study focusses primarily on O VI absorption, we have combined resolved H I components into single absorbers in cases where only one, broad O VI absorber is seen; for example, the pair of H I absorbers at $z = 0.0948$ and 0.0950 toward PKS 1302-102 show a single, broad O VI line and thus have been combined into one absorber. Other cases, where both Lyα and O VI show clear multiple structure, have been treated as separate absorbers.

To test our concordance plot method of determining N and b, we simulated multi-component absorbers with a grid of ~ 100 models varying the column density ratio ($N_1/N_2 = 1 - 10$) and velocity separation ($\Delta v = 0 - 75$ km s^{-1}). We measured the equivalent width of the blended pair of simulated absorbers and treated them as a single absorber without any a priori knowledge of their structure. For a pair of simulated H I absorbers with column densities N_1 and N_2 and line widths b_1 and b_2 separated by Δv, a COG analysis of the blended system yields a combined column density no more than 20% greater than $N_1 + N_2$ and usually substantially better. The derived line width *is* affected by unresolved structure as component separation mimics a larger b value. Nevertheless, we find empirically that $b^2_{\rm COG} \leq b^2_{\rm max} + 0.45\,(\Delta v)^2$ where $b_{\rm max}$ is the larger of the two component linewidths. Multiple components, for instance multiple absorbers within the same galaxy cluster, may mimic a broader single absorber, but the effect is small for line separations of *FUSE* instrumental resolution or less. Total column density is essentially insensitive to blended sub-components via our methods. This result is consistent with that found by Jenkins (1986).

Our COG-derived N and b values for the H I absorbers, along with 1σ limits, are listed in Table 3. In some cases, particularly for weak absorbers, concordance plots yielded no useful information and we adopt N and b from other sources. In most of these cases, we adopt measurements from Lyα-only fits or apparent column measurements quoted in the literature or measured by the Colorado group. In a few cases, we assume $b = 20 \pm 10$ km s^{-1} and derive N based on the observed Lyα equivalent width. These cases are noted in Table 3.

As a further check on the validity of our methods, we checked our $b_{\rm HI}$ and $N_{\rm HI}$ values against published values. There are surprisingly few COG-qualified H I measurements in the literature and we were only able to find 30 H I absorbers for our comparison. Our $N_{\rm HI}$ values are consistent within $\pm 1\sigma$ with published values in 20 out of 30 cases (67%), within $\pm 2\sigma$ in 24 cases (80%), and within $\pm 3\sigma$ in all cases. Doppler width is consistent within $\pm 1\sigma$ in 18 out of 28 cases (64%, two absorbers were disqualified from consideration because they were interpretted as multiple absorbers in the litterature but as a single absorber in this study) and within $\pm 2\sigma$ in 26 cases (93%). We have noted $> 2\sigma$ deviations from published values in Table 3. The median absolute deviance in the sample is $\sim 0.6\sigma$ for both $b_{\rm HI}$ and $N_{\rm HI}$. The two-sided deviance distribution in each case is symetric and consistent with no systematic over- or under-prediction.

3.2. *O VI and C III Analysis*

The O VI doublet does not have enough contrast in $f\lambda$ to use concordance plots to determine accurate columns, nor are both lines detected for many absorbers. Apparent and/or profile-fit column densities and b-values were adopted for these transitions. The equivalent width of absorption lines on the linear part of the curve of growth follows the relation

$$W_\lambda = \left(\frac{\pi e^2}{m_e c}\right)\frac{N f \lambda^2}{c} \qquad (2)$$

while line-center optical depth goes as

$$\tau_0 = \left(\frac{\pi e^2}{m_e c}\right)\frac{N f \lambda}{\sqrt{\pi}\, b}. \qquad (3)$$

Thus an absorbsion line saturates (reaches $\tau_0 = 1$) at equivalent width $W_\lambda({\rm sat}) = (b/c)\sqrt{\pi}\lambda = (153$ mÅ$)\, b_{25}$ where b_{25} is the Doppler parameter in units of 25 km s^{-1}. This corresponds to $N_{\rm HI} = (10^{13.62}$ cm$^{-2})\, b_{25}$ for Lyα. For O VI, saturation occurs at a column density $N_{\rm OVI} \sim (10^{14.09}$ cm$^{-2})\, b_{25}$ and most of our O VI detections are at or below this level (see Figure 1a of Paper I). Similarly, C III saturates at $N_{\rm CIII} \sim (10^{13.35}$ cm$^{-2})\, b_{25}$ which is within the range of our measurements. Any saturation in ionic absorbers is mild at worst, and Voigt profile fits and apparent column measurements are probably indicative of the true values. For upper limit cases, the S/N-based 3σ minimum equivalent width was converted to column density via a curve of growth assuming $b = 25$ km s^{-1}.

Our measured line widths and equivalent widths for the O VI doublet absorbers are listed in Table 4. In cases where both lines of the O VI doublet were detected, an error-weighted mean of the columns was taken as the canonical value. Quoted errors are 1σ uncertainties based on line fits. In some cases, absorption is seen at velocities different from the expected value. Part of the difference is due to the variable *FUSE* wavelength solution and uncertainty in the fiducial Lyα absorber velocity, but $\Delta v > 30$ km s^{-1} probably represents a real kinematic difference. High-Δv cases are noted in Table 4.

C III has only one resonance transition at 977.02 Å in the *FUSE* band, which makes detection more challenging than for the O VI doublet lines. Furthermore, low-redshift C III absorbers must be measured at $\lambda < 1000$ Å where the H_2 line density is high and *FUSE* S/N is low. On the other hand, the short rest wavelength of C III allows absorbers to be measured out to a higher redshift ($z \leq 0.21$) in *FUSE* data. Column densities and b-values for C III were determined in the same way as O VI and are listed in Table 5. In several cases, multiple C III components were seen in an evidently single H I absorber. These were measured separately, and the quantities listed in Table 5 represent the total equivalent width and column for the system.

As a final step in our analysis, we carefully inspected each candidate O VI and C III absorber by hand to verify

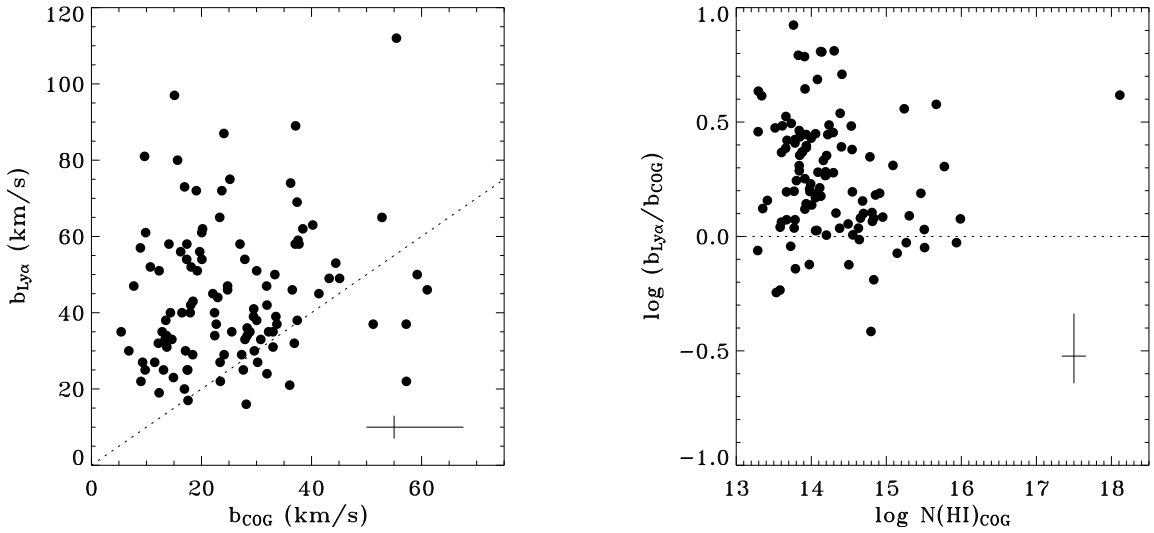

FIG. 2.— (Left) Comparison of line width measured from Lyα lines alone versus curve-of-growth b from our concordance plots. (Right) b value predictive accuracy as a function of $N_{\rm HI}$. There is little correlation between the b measured from concordance plots ($b_{\rm COG}$) and from the Lyα line alone ($b_{\rm Ly\alpha}$), but $b_{\rm Ly\alpha}$ tends to overpredict $b_{\rm COG}$ values. The ratio $b_{\rm Ly\alpha}/b_{\rm COG}$ has a faint dependence on column density, with the widths of stronger absorbers being more accurately predicted by Lyα-only measurements in comparison to lower $N_{\rm HI}$ lines. Median uncertainties are shown in the lower right of each panel.

its existence. Consequently, some detections were downgraded to upper limits because of blending or suspect data features such as flat-fielding issues. In total, we detect 30 C III absorbers and 88 upper limits. O VI is detected in one or both lines of the doublet in 40 absorbers with 84 upper limits.

4. DISCUSSION

4.1. *The Importance of Lyβ*

The majority of the literature on IGM absorption lines, particularly at high redshift, is based on analysis of Lyα lines. A few words of caution regarding this are in order. Our curve-of-growth measurements of $N_{\rm HI}$ and $b_{\rm HI}$ using multiple Lyman lines for each absorber should be more accurate than measurements based on Lyα detections alone; Lyα lines saturate at $\log N_{\rm HI} \sim 13.5$ ($W_{\rm Ly\alpha} \sim 180\, b_{25}$ mÅ). We expect Lyα-only measurements to accurately describe the column and width of weak absorbers where saturation is minimal, but the Lyα-only measurements should grow increasingly inaccurate as saturation and unresolved subcomponents become more substantial. The median $W_{\rm Ly\alpha}$ in our sample is greater than 200 mÅ, so Lyα saturation is a definite concern.

Figure 2a shows no correlation between COG-determined Doppler width, $b_{\rm COG}$, and line-width based on the Lyα absorbers alone, $b_{\rm Ly\alpha}$. In general, $b_{\rm Ly\alpha}$ overpredicts the multi-line $b_{\rm COG}$ by a factor of two or more as seen in Shull et al. (2000), but there is no other correlation. Using high-resolution data, Sembach et al. (2001) found multiple narrow velocity components within the Lyα absorption complex at $z = 0.0053$. Their COG analysis of this system using Lyα-Lyθ lines shows $b = 16.1 \pm 1.1$ km s^{-1} and $\log N_{\rm HI} = 15.85^{+0.10}_{-0.08}$ while Lyα-only measurements give $b = 34.2 \pm 3.3$ km s^{-1} and $\log N_{\rm HI} = 14.22 \pm 0.07$, a factor of two in line width and 43 in column density. Figure 2b shows $b_{\rm Ly\alpha}/b_{\rm COG}$ as a function of $N_{\rm HI}$; the stronger absorbers show less line-width overprediction than the weaker absorbers. However, given the heterogenous nature of the methods used to measure Lyα line widths and column densities, we are hesitant to spend too much effort analyzing their differences.

The differences between curve-of-growth column densities and Lyα-only column densities can be addressed more rigorously. The literature sources listed in Table 2 measure Lyα column density in a variety of ways. We ignore the quoted column density and calculate $N_{\rm HI}$ based only on $W_{\rm Ly\alpha}$ using a single-transition concordance plot and the quoted b value. For absorbers where no line width is quoted, we choose $b = 25$ km s^{-1} based on our COG mean value as discussed below. This gives us a consistent, Lyα-only based column density to compare with our multi-line curve of growth results. Figure 3 shows that Lyα is reasonably accurate in predicting the column densities of weak, unsaturated lines ($\log N \lesssim 13.5$). However, $N_{\rm HI}$ is increasingly underpredicted for stronger, more saturated lines.

A subset of literature sources, including all of the absorbers measured by the Colorado group, determined Lyα-only column densities from profile fits in which $N_{\rm HI}$ and b were free parameters. These are shown in Figure 3 as open triangles. We find that a similar trend is present even in the profile-fit data, although it tends to be more accurate than columns based on $b_{\rm Ly\alpha}$ and $W_{\rm Ly\alpha}$. These points serve to further illustrate the critical importance of higher Lyman lines to the analysis of H I absorbers in the IGM.

The number of absorbers $\mathcal{N}$ as a function of column density $N_{\rm HI}$ follows a power-law distribution $d\mathcal{N}_{\rm HI}/dN_{\rm HI} \propto N_{\rm HI}^{-\beta}$ so that the integrated number distribution $\mathcal{N}(\geq N_{\rm HI}) \propto N_{\rm HI}^{1-\beta}$. Penton, Stocke, & Shull

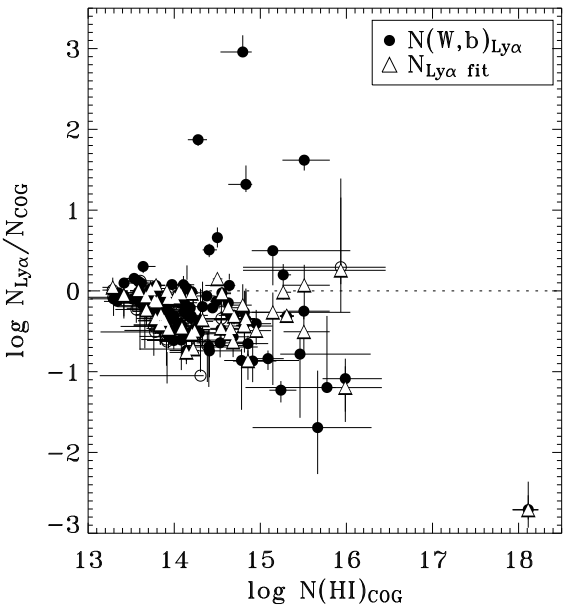

FIG. 3.— A comparison of column density determined from Lyα lines alone vs curve-of-growth column density. $N_{\rm HI}$ determined from $W_{\rm Ly\alpha}$ and Lyα line width (circles) is less than that determined from a COG using multiple Lyman lines. The underprediction generally becomes worse for more saturated Lyα absorbers. A value $b = 25$ km s^{-1} is assumed for any absorbers with no listed Lyα linewidth (open circles). Fitting Lyα lines with Voigt profiles (triangles) generally gives a better match, but still tends to underpredict $N_{\rm HI}$ from a COG.

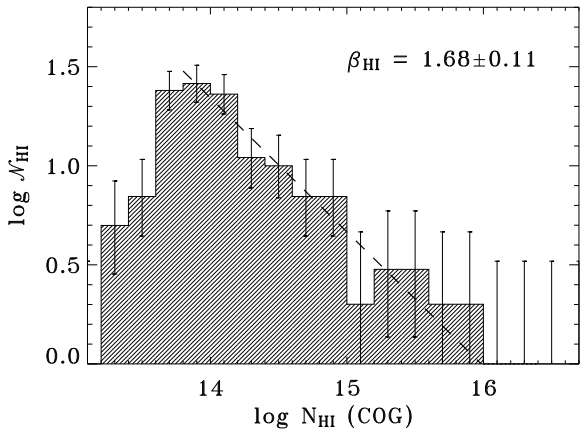

FIG. 4.— The revised distribution of HI absorbers as a function of column density; error bars represent single-sided counting errors (Gehrels 1986). The distribution can be fitted by a power law $d\mathcal{N}_{\rm HI}/dN_{\rm HI} \propto N_{\rm HI}^{-\beta}$ so that $\mathcal{N}(\geq N_{\rm HI}) \propto N_{\rm HI}^{1-\beta}$. We find $\beta = 1.68 \pm 0.11$ for our sample above $N_{\rm HI} = 10^{13.8}$ cm^{-2} (dashed line).

(2004) obtained values of $\beta = 1.65 \pm 0.07$ over the column density range $12.3 \leq \log N_{\rm HI} \leq 14.5$ and $\beta = 1.33 \pm 0.30$ for $14.5 \leq \log N_{\rm HI} \leq 17.5$, based on a similar set of absorbers and an assumed $b = 25$ km s^{-1}. Williger et al. (2006) find $\beta = 2.06 \pm 0.14$ for $\log N_{\rm HI} \geq 13.3$ based on 60 H I absorbers. Our sample is limited to $W_{\rm Ly\alpha} > 80$ mÅ, so much of the lower range in column density is missing when compared to the Penton sample, but we recreate the power-law fits to the distribution using b and $N_{\rm HI}$ values from curves of growth. We find $\beta = 1.85 \pm 0.39$ for the weak absorbers ($13.8 \leq \log N_{\rm HI} \leq 14.5$) and $\beta = 1.50 \pm 0.23$ for the stronger absorbers ($14.5 \leq \log N_{\rm HI} \leq 17.5$) but note that the individual sub-samples are small and may be of reduced statistical significance. This slight steepening of the distribution between Lyα-only and full COG analyses is contrary to what we would expect. Given that Lyα-only measurements tend to underpredict column density relative to full COG analyses as shown in Figure 3, we would expect a flatter distribution, especially for stronger absorbers.

Simulations (Davé et al. 2001) suggest that higher column density absorbers will evolve faster toward lower redshift than low column absorbers through infall and large scale structure formation, thus producing a steeper distribution at $z = 0$. Weymann et al. (1998) find $\beta \approx 1.3$ for $\log N_{\rm HI} > 13.5$ assuming $b = 30$ km s^{-1} for sight lines in the FOS Key Project ($z < 1.3$). We find a considerably steeper distribution in our total sample as shown in Figure 4: $\beta = 1.68 \pm 0.11$ for $\log N_{\rm HI} > 13.8$. Studies of the high-redshift Lyα forest find $\beta = 1.46$ and 1.55 at $z \sim 2.85$ and $z \sim 3.7$, respectively (Hu et al. 1995; Lu et al. 1996; Kim et al. 1997; Davé & Tripp 2001). Our distribution is marginally steeper than the high-redshift samples, but does not agree with the low-redshift FOS sample. The FOS survey is limited to Lyα-only measurements of strong absorbers ($W_{\rm Ly\alpha} \gtrsim 200$ mÅ) and closely-spaced absorbers individually near the detection threshhold may be blended together into an artificially strong single absorber (see e.g. Parnell & Carswell 1988). This would artificially flatten the FOS distribution with respect to more sensitive, higher resolution surveys.

4.2. *C III Absorber Distribution*

The C III detections are not as numerous as O VI detections. There is only one resonant C III transition, and each C III absorber stands a higher chance of being obscured by another line, often H_2. The C III λ977 transition is intrinsically 5.4 times stronger (in $f\lambda$) than O VI λ1032. If intergalactic C/O has a relative abundance ratio equal to that in the Sun, $(\rm C/O)_\odot = 0.5$ (Allende Prieto et al. 2001b), the C III transition would be 2.7 times more sensitive to metal-enriched gas than O VI. Counteracting the intrinsic C III strength is the fact that low-z C III absorbers fall in the less sensitive (SiC) portion of the *FUSE* detectors.

We see C III at the $> 3\sigma$ level in 30 out of 148 Lyα absorbers. To calculate the total redshift pathlength, we employ a method identical to that used for O VI in Paper I. The 3σ minimum equivalent is calculated as a function of wavelength based on signal to noise for each sight line. This minimum equivalent width is translated into $N_{\rm min}(\lambda)$ assuming $b = 25$ km s^{-1}. An absorber is then moved along the spectrum as a function of $z_{\rm abs}$ and the total pathlength is summed as a function of $N_{\rm min}$ for C III (Figure 5a). Detections are binned by column density, and the bins are scaled by $\Delta z(N)$ to produce $d\mathcal{N}_{\rm CIII}/dz$ (Figure 5b). We define the rolloff in the redshift pathlength as the point where $\Delta z(N)$ equals 80% of $\Delta z(\infty)$. This occurs at $\log N_{\rm CIII} = 12.75$, compared to $\log N_{\rm OVI} = 13.35$ (see Figure 3, Paper I).

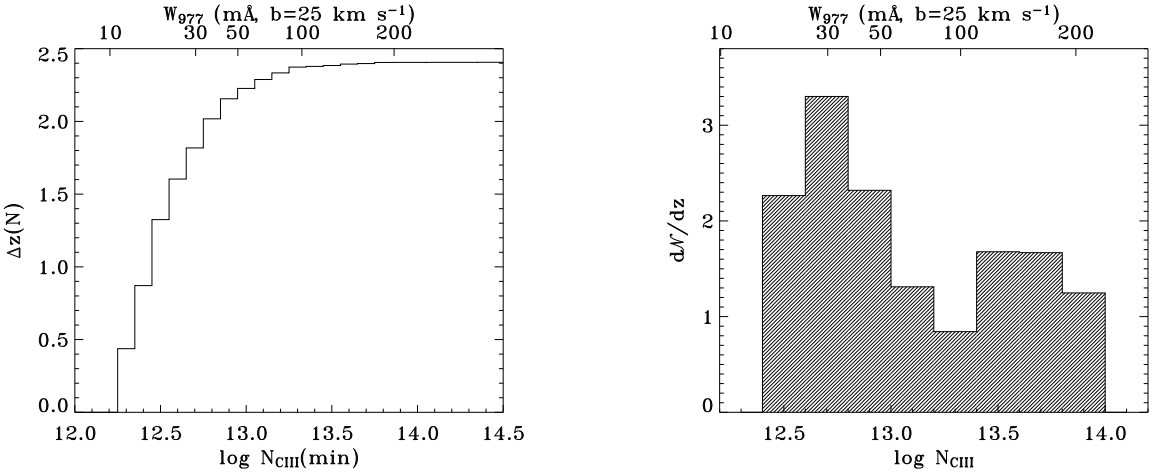

FIG. 5.— The profile of effective redshift versus column density sensitivity $\Delta z(N)$ for C III (left) is used to correct for sample incompleteness in $d\mathcal{N}_{\rm CIII}/dz$ as a function of column density in cm^{-2} (right). The equivalent-width limit for the λ977 line is shown at the top of both figures.

There is little if any literature information on C III absorber statistics. We quote here the integrated line frequency per unit redshift, $d\mathcal{N}_{\rm CIII}/dz$, down to a given equivalent width limit, in parallel with $d\mathcal{N}_{\rm OVI}/dz$ (Paper I and sources therein). Above $W_\lambda = 30$ mÅ, we see 26 C III absorbers over $\Delta z \leq 2.406$, so that $d\mathcal{N}_{\rm CIII}/dz = 12^{+3}_{-2}$. The quoted uncertainties are based on the single-sided 1σ confidence limits of Poisson statistics (Gehrels 1986). Raising the threshold to $W_\lambda > 50$ Å yields 20 C III absorbers and $d\mathcal{N}_{\rm CIII}/dz = 8 \pm 2$. We fit the cumulative distribution in column density assuming a differential power law, $d\mathcal{N}_{\rm CIII}/dN_{\rm CIII} \propto N_{\rm CIII}^{-\beta}$ as we have with O VI (Paper I) and H I (Penton, Stocke, & Shull 2004, this work). We find $\beta_{\rm CIII} = 1.68 \pm 0.04$ for $12.4 < \log N_{\rm CIII} < 13.8$, remarkably similar to $\beta_{\rm HI}$ but not as steep as the O VI distribution. The similarity in $\beta_{\rm HI}$ and $\beta_{\rm CIII}$ is circumstantial evidence that both species are tied to related ionization processes, while the steeper $\beta_{\rm OVI}$ suggests that a different physics is taking place here. We explore the issue of ionizing mechanisms below.

4.3. *The Multiphase IGM*

A central question in the IGM, and one critical to our interpretation of the data, is whether the observed gas is collisionally ionized through shocks and conductive interfaces, photoionized by the ambient QSO radiation field, or some combination of the two. We have usually assumed that O VI is created in shocks between intergalactic clouds (Paper I) and thus traces the WHIM phase. However, an ambient hard UV field incident on very low density gas ($n_H \sim 10^{-5}$ cm^{-3}) can produce a measurable quantity of O VI and other high ions. If this is the case, the observed O VI does not represent a hot phase at all and cannot be used to trace the WHIM.

Davé et al. (2001) argue that the radiation field at $z > 2.5$ was strong enough to ionize a significant amount of the oxygen in the IGM to O VI, but that the ionizing flux at $z < 1$ is too low; QSOs are less common in the modern universe, and the Hubble expansion has spread them to greater average distances diluting the radiation field. Shocks are therefore the likely source of highly ionized gas, either from SN-driven galactic winds, virial shocks associated with large galaxies and clusters, or shocks from infalling clouds outside the virial radius (Birnboim & Dekel 2002; Shull, Tumlinson, & Giroux 2003; Furlanetto, Phillips, & Kamionkowski 2005; Stocke et al. 2005).

On the other hand, Prochaska et al. (2004) analyzed metal lines in six absorbers along the sight line toward PKS 0405-123 on the basis of collisional and photoionization models. They determine that several absorbers are consistent with single-phase collisional ionization under collisional ionization equilibrium (CIE), but that others are better explained with by photoionization from an ambient QSO field. They note, however, that several systems could also be explained with multi-phase ionization models. Similarly, Collins, Shull, & Giroux (2004) analyze absorption lines from many different FUV ions in four high velocity cloud absorbers in the Galactic halo. They conclude that some absorbers show evidence for photoionization while others are more consistent with ionization by shocks. In at least one case, the best explanation was a combination of photo- and collisional ionization. The question of shocks versus photoionization is not yet resolved (Stocke et al. 2005).

Our study does not include enough different ion states for a detailed comparison of each absorber with models. Future work on C IV, Si IV, and Si III absorption in STIS data should constrain observations so that detailed ionization models in can be constructed. However, we can look at H I, C III, and O VI absorber detections to examine the energetics of each set as a specific class as well as the ensemble as a whole.

The absorber detection statistics are instructive. For the purposes of this argument, we define detections as H I absorbers with $\log N_{\rm OVI} \geq 13.2$ (37 out of the 40 total 3σ detections) or $\log N_{\rm CIII} \geq 12.6$ (27 out of 30 total detections). Similarly, we define non-detections as upper limits below the thresholds. This accounts for the top $\sim 90\%$ of detections in each metal ion and counts only upper limits with reasonable data quality. We further narrow the sample to those absorbers with good statistics (detections or non-detections as defined above) in both

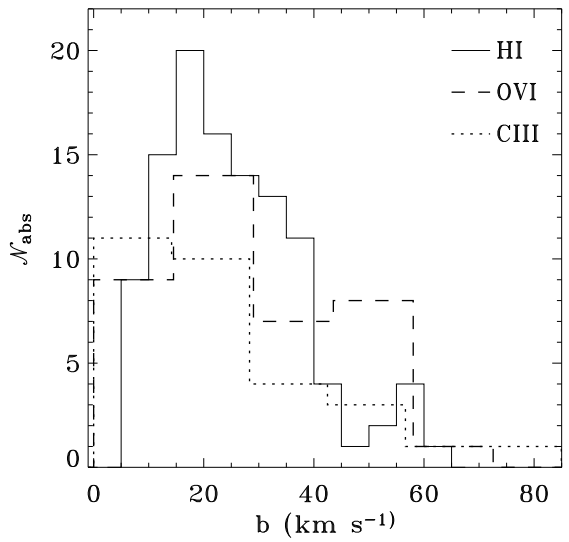

FIG. 6.— Distribution of b values for H I, O VI, and C III absorbers. The $b_{\rm COG}$(HI) values represent COG values while $b_{\rm cor}$(metal) have been corrected for an instrumental resolution of $\Delta V \approx 15$ km s^{-1} ($b_{\rm FUSE} = 9$ km s^{-1}). Mean values are $\langle b_{\rm COG}({\rm HI})\rangle = 25 \pm 13$ km s^{-1}, $\langle b_{\rm cor}({\rm OVI})\rangle = 31 \pm 14$ km s^{-1} and $\langle b_{\rm cor}({\rm CIII})\rangle = 26 \pm 13$ km s^{-1}.

O VI and C III. This gives a sample of 45 H I absorbers with absorption statistics in both metal ions. We detect O VI in 20 absorbers (44%) and C III in 16 (36%), and twelve absorbers (27%) show both O VI and C III. We see H I and O VI without accompanying C III in eight cases (18%), and four absorbers (9%) show H I and C III without O VI. Twenty-one absorbers show neither O VI nor C III.

An important caveat is that our survey for metal absorbers is not a "blind" survey; we look for absorption only near the velocities of known, strong Lyα absorption, and we ignore the possibility of low-ionization metal-line absorbers without H I. Except for highly ionized (X-ray) absorption lines, there is no definitive evidence for such absorption in the low-redshift universe. Thus, we treat $\Delta z_{\rm metal}$ as equivalent to $\Delta z_{\rm HI}$. Furthermore, we assume that our sample of IGM absorbers have H I, C III, and/or O VI which are cospatial but not necessarily well-mixed; we limit velocity separations between any two lines to $\Delta v < 100$ km s^{-1}. We do not have the spectral resolution for detailed kinematic studies of the absorption systems.

4.3.1. *Absorber Line Widths*

The distribution of Doppler line widths is a clue to the temperature (and hence phase) of a species and may help clarify the ionization source. The b values of O VI and C III absorbers both show asymmetric distributions that peak around 20 km s^{-1} and fall off gradually to about 50 km s^{-1}. Unlike the $b_{\rm COG}$ values derived for the H I absorbers, b(metal) includes an instrumental profile. We assume $R = 15,000$ for a *FUSE* resolution of 15 km s^{-1} (Hebrard et al. 2006; Williger et al. 2005) ($b_{\rm FUSE} = 12$ km s^{-1}) and subtract this in quadrature from $b_{\rm metal}$. We find mean values $b_{\rm cor}({\rm OVI}) = 29 \pm 18$ km s^{-1} and $b_{\rm cor}({\rm CIII}) = 23 \pm 18$ km s^{-1} (Figure 6). Median values are smaller by ~ 3 km s^{-1} in both cases.

Thermal line widths for O VI and C III at their peak CIE temperatures are $b_{\rm therm} \sim 17$ km s^{-1} and $b_{\rm therm} \sim 10$ km s^{-1}, respectively; the observed line widths are consistent with multiple photoionized components or thermal broadening of a collisionally ionized component. Regardless of temperature, some of the observed width must be due to turbulence, multiple components, or Hubble expansion within extended, diffuse clouds (Weinberg, Katz, & Hernquist 1998; Richter et al. 2004). Heckman et al. (2002) argue that, since the fractional abundance of O VI in CIE is a function of temperature peaked at $T_{\rm max} = 10^{5.45}$ K, O VI preferentially is found at or near its CIE peak temperature as gas cools from higher temperatures and $T \approx T_{\rm OVI} = 10^{5.45}$ K is a good approximation. (In non-equilibrium cooling, the gas could start out at 10^6 K or hotter and cool below $T_{\rm max}$.) If $T \approx T_{\rm max}$, subtracting a thermal line width component at $T_{\rm OVI}$ leaves $b_{\rm turb}({\rm OVI}) = 23$ km s^{-1}, equivalent to the Hubble broadening for a quiescent cloud $\sim 330\, h_{70}^{-1}$ kpc across. Of course, we do not know the extent of turbulent velocities in IGM clouds, so this should be considered an upper limit for the typical WHIM absorber scale (see discussion in § 4.3.4 below).

Beryllium-like C III ($1s^2 2s^2$) has two valence electrons and thus has a broader range of temperatures over which it has a significant ionization fraction in CIE. Because little theoretical work has been done on C III ionization fraction in the non-equilibrium conditions likely to be present in the IGM, we assume that its peak CIE abundance temperature, $T_{\rm CIII} = 10^{4.85}$ K, is characteristic of any collisionally ionized C III absorbers. This corresponds to $b_{\rm thermal}({\rm CIII}) = 10$ km s^{-1}. Photoionized C III would have a lower temperature ($\sim 10^4$ K) and much smaller thermal correction of $b_{\rm therm} \sim 4$ km s^{-1}. Thus, $b_{\rm turb}({\rm CIII}) = 21 - 23$ km s^{-1}, depending whether C III is collisionally ionized or photoionized, similar to $b_{\rm turb}$(OVI).

Hydrogen line width is more sensitive to temperature than the metal ions. The distribution of $b_{\rm COG}$(HI) is peaked near 20 km s^{-1}, but it has non-negligible contribution from values out to 35 km s^{-1} implying contributions from turbulence, Hubble expansion, or unresolved multi-component structure. The mean value is 25 ± 13 km s^{-1}. Since $b_{\rm COG}$(HI) is derived from equivalent widths, it is independent of instrumental resolution and represents only the quadratic sum of thermal and turbulent components. If the entire $b_{\rm COG}$(HI) is thermal in nature (which is unlikely), this represents gas with a temperature of $\log T = 4.6^{+0.4}_{-0.6}$ using 1σ errors to define a temperature range. The thermal width of a line at typical H I temperatures of 10^4 K accounts for $b_{\rm therm}({\rm HI}) = 13$ km s^{-1} leaving $b_{\rm turb}({\rm HI}) = 21$ km s^{-1}, similar to that seen in C III and O VI.

It may be that the observed H I absorption comes not from a warm phase, but from the WHIM. Richter et al. (2004, 2005) note that the neutral fraction of hydrogen at WHIM temperatures in CIE is very small ($< 10^{-5}$). However, a large total hydrogen column density ($\log N_{\rm H} \sim 19$) of low-density gas spread over 300 kpc will still produce measurable absorption in H I. These

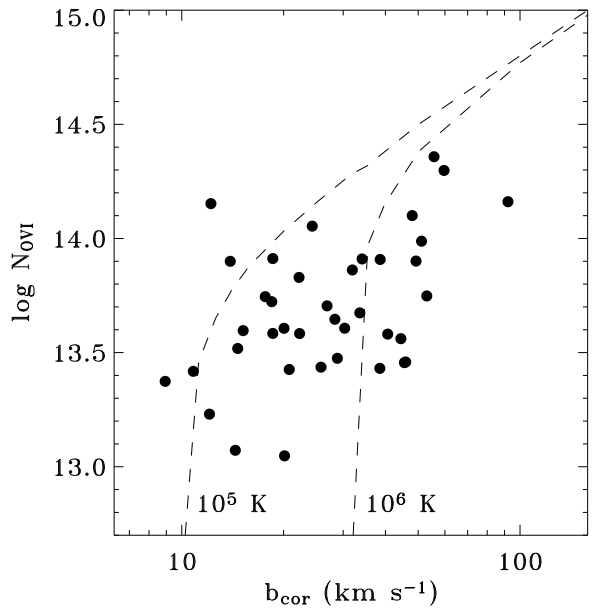

FIG. 7.— Theoretical models show a relationship between $b_{\rm OVI}$ and $N_{\rm OVI}$ (cm^{-2}) across a wide range of astrophyical systems. The dashed lines show the predictions of (Heckman et al. 2002) for temperatures of 10^5 K and 10^6 K. We see no such correlation in IGM O VI absorbers in our 40 absorbers (solid circles), although they do tend to fall within the bounds of WHIM temperature curves.

systems would be distinguishable from non-WHIM H I absorbers by their large thermal b values. For purely thermal line-widths, we would expect $b_{\rm HI} \sim 70$ km s^{-1} for $T = 10^{5.5}$ K. Richter et al. (2005) report on 26 features in the sight lines of four AGN which they identify as broad Lyα absorbers. We see no absorbers with $b_{\rm HI} > 70$ km s^{-1}, but there are 8 absorbers with $b_{\rm HI} > 45$ km s^{-1}. These may be WHIM H I or unresolved multiple components as noted above. However, the majority of the H I lines show narrow line widths, inconsistent with hot H I, and we are forced to conclude that H I traces a warm neutral and moderately ionized phase in most cases. The issue of gas temperature is still open for C III and O VI, at least based on line widths.

Heckman et al. (2002) argue that line width is directly related to the velocity of the postshock gas and that all O VI absorption systems, regardless of scale and origin, follow a simple relationship between line width and column density. The exact relationship depends on the temperature of the O VI gas, and comes about as hot gas cools radiatively through the temperature regime in which O VI is abundant and can be detected. Observational data from systems as diverse as starburst galaxies ($N_{\rm OVI} \sim 10^{15}$ cm^{-2}) and Galactic disk absorbers ($N_{\rm OVI} \sim 10^{13-14}$ cm^{-2}) show good agreement with theoretical predictions (see Heckman et al. 2002, Figure 1). The eight IGM data points in that Figure are located at the lower end of the column density range and show the most spread of any physical system.

With 40 O VI detections in the IGM, we can improve the statistics immensely. Figure 7 shows the relationship between corrected $b_{\rm cor}$(OVI) and $N_{\rm OVI}$. The IGM O VI absorbers from our sample do not show the same correlation as absorbers in other physical situations, although the data points generally fall between the temperature curves corresponding to 10^5 K and 10^6 K. The lack of correlation may be due to unresolved multiple components in the IGM absorbers or Hubble broadening. However, blended absorbers would show a higher b and be located farther to the right than they should. It is clear that many of the observed IGM systems already show smaller b than absorbers from different systems.

The explanation may be that Heckman et al. (2002) rely on complete radiative cooling in their model to derive the $N - b$ correlation. All the other systems in question have physical densities several orders of magnitude higher than expected for the IGM ($n_H \sim 10^{-5}$ cm^{-3}) and thus the cooling time is comparatively short. Diffuse IGM clouds can have cooling times comparable to or longer than H_0^{-1} (Collins, Shull, & Giroux 2004; Furlanetto, Phillips, & Kamionkowski 2005). Once a given species is out of ionization equilibrium, it becomes harder to use its line width as a gauge of temperature. For example, a gas that cools faster than it recombines could have a narrower line width than derived under CIE assumptions.

4.3.2. *Column Density Ratios*

In Paper I we demonstrated a lack of correlation between $N_{\rm OVI}$ and $N_{\rm HI}$. $N_{\rm HI}$ varies over a range of nearly 1000 in our sample of low-column systems and the Lyman limit systems (LLSs). Damped Lyα absorbers (DLAs) seen in other sight lines (Lopez et al. 1999; Jenkins et al. 2003) extend the range of $N_{\rm HI}$ over at least eight orders of magnitude. In contrast, $N_{\rm OVI}$ shows a variation of only a factor of 30 in our sample and has never been detected at columns of greater than a few $\times 10^{15}$ cm^{-2} (Heckman et al. 2002). This small range of $N_{\rm OVI}$ compared with $N_{\rm HI}$ manifests itself as a good correlation of the "multiphase ratio" $N_{\rm HI}/N_{\rm OVI}$ with $N_{\rm HI}$ (see Paper I, Figure 1).

The column density of C III shows a similar dynamic range (1.5 dex) to $N_{\rm OVI}$ (Figure 8a). Unlike $N_{\rm OVI}$, $N_{\rm CIII}$ does show some degree of correlation with $N_{\rm HI}$. The $N_{\rm HI}/N_{\rm CIII}$ multiphase ratio (Figure 8b) is highly correlated in a similar manner as $N_{\rm HI}/N_{\rm OVI}$ (Paper I) for weak absorbers ($N_{\rm HI} \lesssim 10^{14.5}$ cm^{-2}), but the scatter becomes greater and the trend appears to level off for stronger absorbers.

It should be noted that a positive slope in multiphase ratio as a function of $N_{\rm HI}$ (Figure 8b and Paper I, Figure 1b) is *not* a metallicity effect (which would show a negative slope reflecting higher H I fractions for higher-$N_{\rm HI}$, metal-enriched gas). We would also expect enriched material to be associated with galaxy outflows more than "void" IGM absorbers. Stronger Lyα absorbers are preferentially seen closer to galaxies than are weak absorbers (Penton, Stocke, & Shull 2004).

The lack of correlation in O VI is a strong indicator that photoionization is not the principal ionizing mechanism of O VI in the IGM. If a species is the product of photoionization, its column densities should be roughly proportional to that of hydrogen in the optically thin limit. We would expect a similar dynamic range and correlation in column density, seen as a horizontal trend in a multiphase plot. $N_{\rm CIII}$ does show correlation with $N_{\rm HI}$, but the dynamic ranges are still substantially dif-

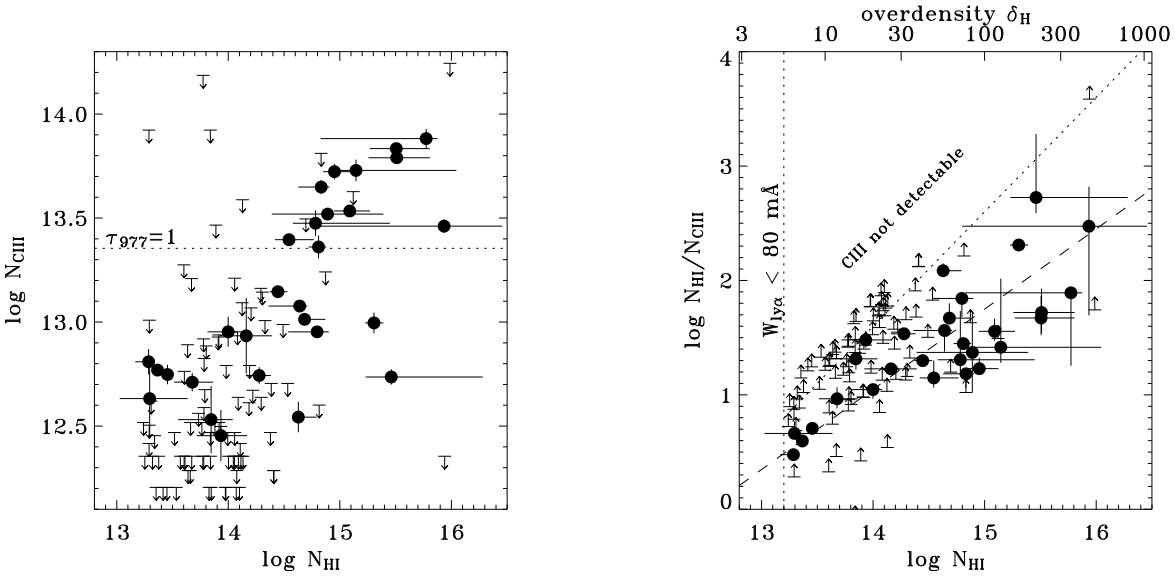

FIG. 8.— Comparison of $N_{\rm HI}$ and $N_{\rm CIII}$ (left) and C III multiphase ratio vs. $N_{\rm HI}$ (right) for 30 IGM absorbers (circles) and 88 upper limits (arrows), similar to O VI analysis (Figure 1 of Danforth & Shull (2005)). The H I and C III absorbers show a good correlation at low column density, implying that the ionization processes are coupled. Higher column absorbers show considerably more scatter. Overdensity $\delta_{\rm H} \equiv 20 N_{14}^{0.7}(10^{-0.4z})$ is shown on the top axis (see (see Davé et al. 1999), and approximate detection limits for H I and C III are shown as dotted lines in the right panel.

ferent.

Photoionization may play a major role in C III production, but its signature proportionality to H I and wide dynamic range in column density may be masked by the discrepancy between apparent and true column density (as discussed above for Lyα lines). C III λ977 is a strong transition and reaches $\tau_0 = 1$ at $\log N_{\rm CIII} = 13.35$ (for $b_{\rm CIII} = 25$ km s^{-1}). Forty percent of the C III detections are at or above this column density. Conversely, the strongest C III absorbers show line-center apparent optical depths $\tau_{\rm a} \gtrsim 2.0$. The distribution of $N_{\rm CIII}$ may be truncated at higher columns by optical thickness, and the true column density distribution may be even shallower than shown in Figure 5.

The O VI doublet transitions are not as strong as C III λ977 and O VI λ1032 reaches $\tau_0 = 1$ at $\log N_{\rm OVI} = 14.09$ (for $b_{\rm OVI} = 25$ km s^{-1}), stronger than all but 12% of the absorbers. The highest apparent optical depth $\tau_{\rm a}$ at line center in our sample is $\tau_{\rm a} \approx 1.5$ and most are at $\tau_{\rm a} < 1$. It seems safe to say that none of the O VI absorbers are optically thick and that the observed upper limit on column density is not a saturation effect. Therefore, we must be seeing some physical regulation mechanism on $N_{\rm OVI}$.

4.3.3. *Single-Phase IGM Models*

Even though we lack the range of ionic states to perform detailed comparisons with ionization models, we can still compare the range of observed values in a few lines with predicted behavior. To this end, we constructed a grid of photoionization models with CLOUDY v96.01 (Ferland et al. 1998). An AGN ionizing continuum (Korista et al. 1997) illuminated a cloud 400 kpc thick at a distance of 10 Mpc from the absorber. This scale is on the order of the scale predicted by our Hubble broadening arguments ($r \lesssim 300$ kpc) and $d\mathcal{N}/dz$ calculations presented below ($r \sim 400$ kpc). The number density n_H and metallicity Z of the cloud were varied between 10^{-6} cm^{-2} and 10^{-4} cm^{-3} ($\delta = 5 - 500$ at $z \approx 0$) and $Z = 0.01 - 1\,Z_\odot$. The luminosity of the illuminating AGN was varied to provide specified ionization parameters ($U = \phi/n_{\rm H}c$) $\log U = -5$ to 0, equivalent to scaling the luminosity of the AGN, and the steady-state temperature was varied between 10^4 K and 10^7 K, the upper end of the WHIM temperature range. The low end of the temperature scale is approximately equal to the photoexcitation temperature and thus approximates a pure-photoionization model similar to those of Donahue & Shull (1991), while the low-ionization end of the grid approximates a purely collisional system in ionization equilibrium equivalent to Sutherland & Dopita (1993). In this way we simulated a single-phase system with both collisional and photoionization processes in effect. Ion fractions for hydrogen, carbon, and oxygen were calculated as well as predicted column densities for H I, O VI, and C III.

Photoionization of H I and C III depends on the shape of the ionizing spectrum in the 1-4 Ryd range, where the ambient radiation field is fairly well known. However, O VI is produced by photons of $E \geq 114$ eV (8.4 Ryd) and typical AGN continua in this region are not as well determined. In our models, we assume a power-law continuum in the EUV region; $I_\nu \propto \nu^{-\alpha}$. The default CLOUDY AGN spectrum (Korista et al. 1997) uses $\alpha = 1.4$, while recent studies find that the soft X-ray continuum follows a steeper power law with $\langle\alpha\rangle \sim 1.8$. We adopt $\alpha = 1.8$ between 1 Ryd and 22 Ryd (300 eV) for our ionizing spectrum. This provides less flux capable of photoionizing O VI and increases the ionization parameters required to photoionize O VI.

Figure 9 shows how observed column density ratios (shaded ranges) compare with those from our model grid. First we calculate the model multiphase ratios $(N_{\rm HI}/N_{\rm OVI})_{\rm model}$ and $(N_{\rm HI}/N_{\rm CIII})_{\rm model}$. These are plot-

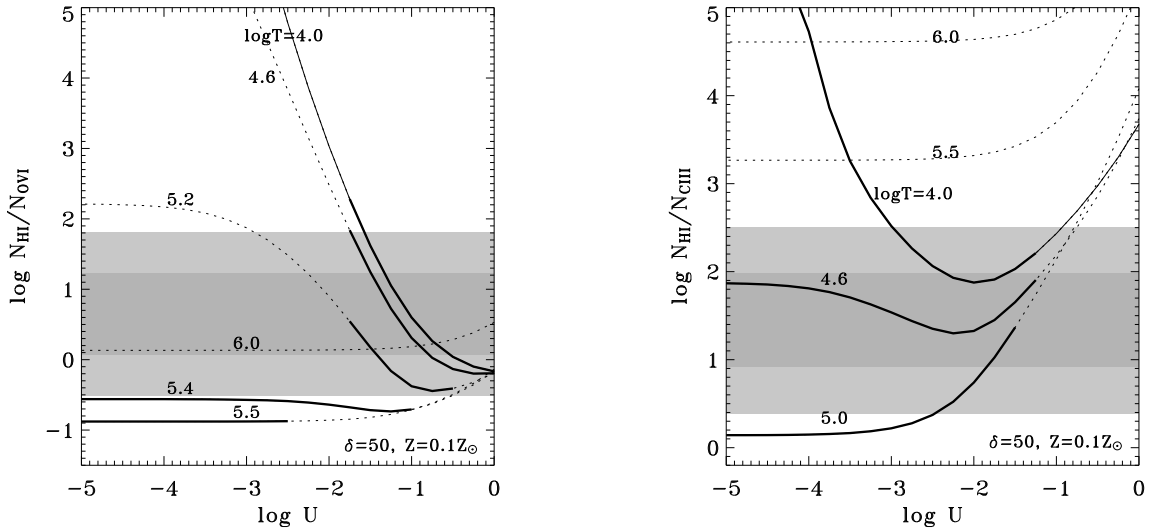

FIG. 9.— The dependence of $(N_{\rm HI}/N_{\rm OVI})_{\rm model}$ (left) and $(N_{\rm HI}/N_{\rm CIII})_{\rm model}$ (right) on ionization parameter U and temperature T in CLOUDY models of the IGM. Models were calculated over a grid of ionization parameters, assuming a fixed temperature set by collisional heating. In the left panel, we see the behavior of $(N_{\rm HI}/N_{\rm OVI})_{\rm model}$ as a function of ionization parameter and temperature assuming $\delta = 50$ ($n_H = 10^{-5}$ cm^{-3}) and $Z = 0.1\,Z_\odot$. The solid line represents the low-temperature case ($T = 10^4$ K, equivalent to a pure photoionization model) and other curves represent photoionization plus steady-state temperature models of different temperatures. Models with detectable columns of both H I and O VI ($\log N_{\rm HI} > 13.2$, $\log N_{\rm OVI} > 13.0$) are shown as thick, solid curves. The shaded bar shows the 1σ (dark) and 2σ range of observed $N_{\rm HI}/N_{\rm OVI}$. The right panel shows the equivalent plot for $(N_{\rm HI}/N_{\rm CIII})_{\rm model}$ and observed values of $N_{\rm HI}/N_{\rm CIII}$. From these, we can severely limit the allowed parameter space for a single-phase IGM absorber.

ted as a function of U for several different temperatures for the intermediate metallicity and density case: $\delta = 50$ ($n_H = 10^{-5}$ cm^{-3}) and $Z = 0.1\,Z_\odot$. Changes in metallicity move the curves up and down linearly. Changes in number density have no effect on line ratios. To further constrain the interpretation, we consider only models that produce column densities above the detection limits of this survey: $\log N_{\rm HI} > 13.2$, $\log N_{\rm CIII} > 12.5$, and $\log N_{\rm OVI} > 13.0$, shown in Figure 9 as thick, solid lines.

We see that several models generate multiphase ratios in the range of the observed quantities (shaded). Either high-ionization ($\log U \gtrsim -2$) or very specific temperatures and low metallicity ($T = 10^{5.4} - 10^{5.5}$ K, $Z < 0.1 Z_\odot$) are required to match observed values of $N_{\rm HI}/N_{\rm OVI}$. An ionization parameter of order $U \sim 10^{-2}$ is feasible given a low-z hydrogen ionizing flux $\Phi_{\rm ion} = 3400$ photons cm^{-2} s^{-1} (Shull et al. 1999) and $n_{\rm H} = 10^{-5}$ cm^{-3}, however the $N_{\rm HI}/N_{\rm CIII}$ observations require low ionization and low temperatures ($\log U \lesssim -2$, $T \lesssim 10^5$ K). No single-phase model can account for both the observed O VI and C III absorbers.

To visualize this in another way, we show the area of U-T parameter space for which $(N_{\rm HI}/N_{\rm OVI})_{\rm model}$ and $(N_{\rm HI}/N_{\rm CIII})_{\rm model}$ are within the observed ranges (Figure 10). Models that produce $N_{\rm HI}/N_{\rm OVI}$ within the observed range and which have column densities greater than the observed threshholds are shown as blue hatching. Modeled values within $\pm 1\sigma$ of the mean observed $N_{\rm HI}/N_{\rm OVI}$ are shown in dense hatching, while those within $\pm 2\sigma$ are shown in a less dense pattern. The equivalent allowed parameter space for $N_{\rm HI}/N_{\rm CIII}$ is shown in red. There is very little overlap of the two allowed regions (denoted by black contours) in Figure 10. A single-phase IGM with both O VI and C III detections is unlikely if not actually impossible given our models.

The collisional ionization model is not without its own problems, however. The time required to cool a diffuse plasma at WHIM temperatures can be approximated as

$$t_{\rm cool} \sim \frac{\frac{3}{2}kT}{n_{\rm H}\Lambda(T)} \sim (2.1\ {\rm Gyr})\frac{T_6}{n_{-4}\Lambda_{-22.5}}\ , \qquad (4)$$

where T_6 is the electron temperature in units of 10^6 K, n_{-4} is the electron density in units of 10^{-4} cm^{-3}, and $\Lambda_{-22.5}$ is the cooling rate coefficient in units of $10^{-22.5}$ erg cm^3 s^{-1}, typical of $Z = 0.1 - 0.3 Z_\odot$ gas (Sutherland & Dopita 1993). For $n = 10^{-5}$ cm^{-3} (an overdensity $\delta = 50$ at $z = 0$) and $Z = 0.1\ Z_\odot$, a 10^6 K plasma will only cool in $\sim$ 20 Gyr. Modifying the metallicity, density, or temperature will change $t_{\rm cool}$, but any reasonable set of IGM parameters will produce a minimum cooling time of a few Gyr. Non-equilibrium calculations (Rajan & Shull 2005; Furlanetto, Phillips, & Kamionkowski 2005) show qualitatively the same conclusion: hot gas at low densities stays hot for a very long time. The frequency of shocking events (either cloud collisions or SN feedback shocks) required to maintain WHIM temperatures is fairly low. Indeed, it becomes impressive that shock-heated IGM gas can cool enough to produce a significant O VI fraction at all. Shocks will increase $n_{\rm H}$ as well as T, but compression from an adiabatic shock can only account for a factor of 4 in density and only a small reduction in $t_{\rm cool}$.

The cooling is dominated (for $Z > 10^{-2} Z_\odot$) by metal ion emission lines (primarily iron) at temperatures below 10^7 K. At lower temperatures, C III and C IV are some of the strongest coolants. As temperatures reach $T <$

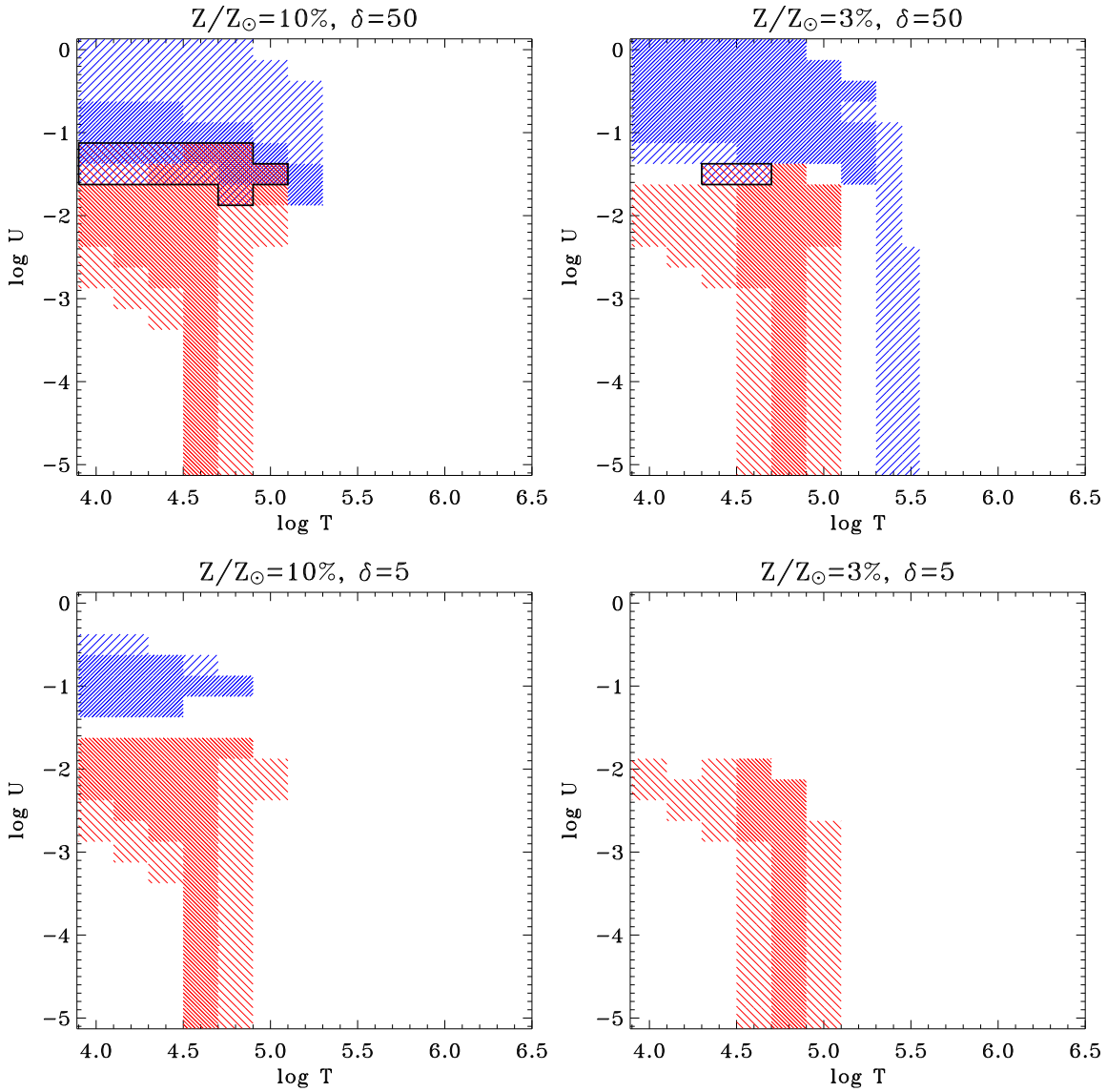

FIG. 10.— Parameter space for which predicted column-density ratios fall within observed ranges. Observationally allowed H I/O VI parameter space is shown in blue for the $\pm1\sigma$ (dense hatching) and $\pm2\sigma$ observed ranges. H I/C III solutions are shown in red, and the overlap regions where both line ratios are within observed limits are noted with a black contour. Model overdensity δ and metallicity are shown above each panel. We see that the overlap region is small for a single-phase IGM model.

10^5 K, C III becomes the dominant carbon ion and the gas cools rapidly. Thus, C III is a transient ion in the cooling column of post-shock gas. Because the shocked IGM takes a long time to cool to C III (and cools further to C II), the presence of strong C III absorption suggests a source from photoionization, not from cooling shocks. Certainly O VI and C III are not simultaneously present in the same gas under CIE conditions.

4.3.4. *Multiphase IGM Models*

Single-phase models can potentially explain the absorbers for which we detect either O VI or C III, but they cannot explain the twelve absorbers for which we see both O VI *and* C III. Is a multiphase, collisionally ionized system physically feasible? We postulate a shock generated by either a cloud collision (such as infall of material onto a filament) or a SNe-driven galactic outflow propagating through a metal-enriched intergalactic cloud. We then investigate whether this model qualitatively reproduces the observed O VI and C III detections.

Since $t_{\rm cool}$ is so long, we cannot assume that post-shock material will have a significant column of low ions. Any C III and other low-ions must come from preshock gas. If the crossing time is long enough, there can be unshocked gas available to provide the low ionization column seen in the observations. We choose a shock velocity of ~ 200 km s^{-1} and calculate the crossing time by estimating a typical IGM absorber scale.

We can estimate typical IGM absorber scale via low-z detection statistics;

$$\frac{d\mathcal{N}}{dz} = n_0(>L)\ (\pi r_0^2)\ \frac{c}{H_0}\ , \qquad (5)$$

where $n_0(>L)$ is the number density of galaxies brighter than a certain minimum luminosity and πr_0^2 is the typical

absorber cross section. We use a Schechter luminosity function

$$\phi(L)dL = \phi_*(L/L^*)^{-\alpha}\ e^{-L/L^*}\ (dL/L^*)\ , \qquad (6)$$

and integrate down to luminosity L. In the special case of $\alpha = 1$, typical of the faint-end slope, the integral becomes the first exponential integral E_1;

$$n_0(>L) = \phi_* \int_L^\infty (L/L^*)^{-1}\, e^{-L/L^*}\, \frac{dL}{L^*}$$
$$= \phi_*\, E_1(L/L^*). \qquad (7)$$

Recent results from the Sloan Digital Sky Survey (SDSS Blanton et al. 2003) give $\phi_* = 0.0149\ h^3$ Mpc^{-3} or $\phi_* = 5.11\times10^{-3}\ h_{70}^3$ Mpc^{-3}. We use $d\mathcal{N}_{\rm OVI}/dz = 17\pm3$ for $W_\lambda > 30$ mÅ (Danforth & Shull 2005) and find that $r_0 = (1060\pm100)\ h_{70}^{-1}$ kpc for L^* galaxies. However, it is likely that the IGM is enriched preferentially by smaller galaxies (Stocke et al. 2005). If we integrate down to $L = 0.1L^*$, we find $r_0 = (370\pm30)\ h_{70}^{-1}$ kpc, a size scale in reasonable agreement with inferred distances of metal distributions from nearest-neighbor galaxies (Stocke et al. 2005). Adjusting ϕ_* downward by 1/3, to account for ellipticals that may not have outflows, we find that r_0 increases by $\sim 20\%$. This analysis assumes a uniform distribution of galaxies. Tumlinson & Fang (2005) find similar scales with $r_0 = 750$ kpc and $r_0 = 300$ kpc for L^* and $0.1L^*$ limits based on actual galaxy distributions from SDSS.

A typical IGM absorber scale of $\sim 400\ h_{70}^{-1}$ kpc also agrees with Lyα forest cloud sizes inferred from photoionization modeling (Shull et al. 1998; Schaye 2001; Tumlinson et al. 2005) and with our rough upper limit on cloud scale based on Hubble broadening of H I absorption lines. Observations of quasar pairs give results not inconsistent with our derived value. The quasar pair LBQS 1343+264 A/B shows characteristic $r_0 \sim 300\ h_{70}^{-1}$ at $z \sim 2$ (Bechtold et al. 1994; Dinshaw et al. 1994). At lower redshift, Young, Impey, & Foltz (2001) find that a coherence length between Lyα absorbers of 500–1000 kpc at $0.4 < z < 0.9$ in a rare triple QSO system.

The crossing time for a 400 kpc cloud by a 200 km s^{-1} shock is 2 Gyr, which is of the same order as the WHIM cooling time. Assuming that IGM absorbers are associated with dwarf galaxies and that shocking events are infrequent, it is perfectly feasible that unshocked, photoionized material would exist to provide the observed C III column density along AGN sight lines, while shocked material could provide the observed O VI.

We can now revisit the different samples of absorbers introduced in § 4.3. The 12 absorbers with both O VI and C III detections can most plausibly be understood as multiphase absorbers. Column densities and line widths show no correlation and are not easily explained with a single-phase photoionized-plus-collisional system. Our sight lines pass through both quiescent photoionized and shocked regions, and we are unable to kinematically differentiate the two phases in the spectra. The two metal ions occupy different temperature and ionization parameter regimes and are found in physically distinct parts of the absorber. Likely the H I absorption is associated with the cooler, photoionized phase, since $b_{\rm HI} \lesssim 40$ km s^{-1} in most cases.

There are eight absorbers with H I and O VI detections and good C III non-detections. These systems may be large, diffuse, photoionized clouds with a high ionization parameter ($\log U > -2$), sufficient to produce O VI by photoionization, and high enough that carbon would be ionized to C IV. The small fraction of neutral hydrogen at this high ionization parameter would show the narrow thermal profiles observed in our H I sample. Equivalently, these systems can be interpreted as two-phase systems with a shocked, WHIM phase (probed by O VI) and an unshocked, photoionized phase observed in H I. The small range of $N_{\rm OVI}$ compared to $N_{\rm HI}$ and the lack of correlation between the two species in column density and β suggests the latter, multiphase interpretation. A broad, WHIM component in H I may be masked by stronger narrow components or be below the detection threshhold of our data.

The four systems with H I and C III detections and O VI non-detections are likely photoionized. CIE cooling is extremely fast at $T < 10^5$ K, and we do not expect that $\sim 10\%$ of the total metal absorbers would be observed during the relatively brief period during which C III is collisionally ionized. The photoionization interpretation provides us with an upper limit to the ionization parameter ($U \lesssim 10^{-2}$) and we must therefore posit that, for this population of absorbers at least, $n_{\rm H} \gg 10^{-5}$ cm^{-3} or that the metagalactic ionizing radiation field is weaker than expected from models.

The 21 absorbers with neither O VI nor C III are likely collisionally ionized to $T > 10^6$ K or metal-poor systems ($Z < 10^{-2} Z_\odot$). The lack of broad H I absorption makes the high-temperature interpretation implausible, and purely photoionized clouds with even modest enrichment should show measurable C III. Stocke et al. (2005) investigate our detection statistics more thoroughly and catalog nearest-neighbor galaxies for each absorber. They find that the Lyα detections with no metal lines tend to show larger nearest-neighbor distances than those with metal line detections. Williger et al. (2006) find stronger clustering between Lyα systems and galaxies for higher $N_{\rm HI}$ systems over larger velocity scales. These results suggest that the metal-enrichment explanation is the most likely.

4.4. *Metallicity of the IGM*

In Paper I, we found good agreement between our observed distribution of $d\mathcal{N}_{\rm OVI}/dz$ and the cosmic evolution models of Chen et al. (2003) at $\sim 10\%$ metallicity. We also derived $Z_{\rm O} \approx 0.09\, Z_\odot\, (f_{\rm OVI}/0.2)^{-1}$ based on the $N_{\rm HI}/N_{\rm OVI}$ multiphase plot, where $(f_{\rm OVI}/0.2)$ is a normalized ionization fraction of O VI in units of the CIE peak value of 20%. Our value of 9% is consistent with the canonical 10% value assumed in many sources (e.g., Savage et al. 2002; Tripp, Savage, & Jenkins 2000).

We determine $(C/H)_{\rm IGM}$ via the H I/C III multiphase data using the same formalism as Paper I,

$$\left\langle \frac{N_{\rm C}}{N_{\rm H}} \right\rangle = \left\langle \frac{N_{\rm CIII}}{N_{\rm HI}} \right\rangle \times \left(\frac{f_{\rm HI}}{f_{\rm CIII}} \right), \qquad (8)$$

where $f_{\rm HI}$ and $f_{\rm CIII}$ are the ionization fractions of those two species. We fit the C III multiphase plot (Figure 8b) as a power law

$$\left\langle \frac{N_{\rm HI}}{N_{\rm CIII}} \right\rangle = C_{14}\, N_{14}^{\alpha}\ , \qquad (9)$$

where N_{14} is the H I column density in units of 10^{14} cm^{-2} and C_{14} is a scaling constant. The best-fit parameters are similar, whether we use the low-$N_{\rm HI}$ half of the C III absorber sample or the entire range of $N_{\rm HI}$: for $\log N_{\rm HI} < 14.5$, $\alpha = 0.73 \pm 0.08$, $C_{14} = 1.06 \pm 0.04$; for the entire sample, $\alpha = 0.70 \pm 0.03$, $C_{14} = 1.05 \pm 0.02$. We adopt the first set of values here, but note that it makes little difference. The mean absorber redshift in our C III sample is $\langle z_{\rm abs} \rangle \approx 0.1$.

We also make use of an empirical relationship from Davé et al. (1999) relating the baryon overdensity, $\delta_{\rm H}$, to H I column density

$$\delta_{\rm H} \equiv \frac{n_H}{(1.90 \times 10^{-7}\ {\rm cm}^{-3})\,(1+z)^3} \tag{10}$$

$$\approx 20\, N_{14}^{0.7}\, 10^{-0.4\,z}\ . \tag{11}$$

Combining Eqs. (9) and (11) and substituting the appropriate constants from the fit, we find

$$\left\langle \frac{N_{\rm HI}}{N_{\rm CIII}} \right\rangle = 26.6\ \delta^{1.04}\ . \tag{12}$$

The neutral hydrogen fraction $f_{\rm HI}$ in Eq. 8 can be derived from case-A photoionization equilibrium in a low density gas:

$$f_{\rm HI} = \frac{n_e \alpha_H^{(A)}}{\Gamma_H} = 4.74\, n_H\, T_4^{-0.726}\, \Gamma_{-13}^{-1}$$

$$= 9.01 \times 10^{-7}\, \delta_{\rm H}\, (1+z)^3\, T_4^{-0.726}\, \Gamma_{-13}^{-1}\ , \tag{13}$$

where T_4 is the temperature in units of 10^4 K and Γ_{-13} is the H I photoionization rate in units of 10^{-13} s^{-1}. The C III ionization fraction is harder to handle analytically. We take $f_{\rm CIII} \approx 0.8$ since this is roughly its maximum value under both CIE and the photoionization modeling of Donahue & Shull (1991). Substituting Eqs. (12) and (13) into Eq (8), we get

$$\left\langle \frac{N_{\rm C}}{N_{\rm H}} \right\rangle = (2.89 \times 10^{-5}) \left(\frac{f_{\rm CIII}}{0.8} \right)^{-1} \delta_H^{-0.04}\, T_4^{-0.726}\, \Gamma_{-13}^{-1}$$

$$Z_{\rm C} = (0.12\, Z_\odot) \left(\frac{f_{\rm CIII}}{0.8} \right)^{-1}\ , \tag{14}$$

using $({\rm C/H})_\odot = 2.45 \times 10^{-4}$ (Allende Prieto et al. 2001a). Our value $Z_{\rm C} = 12\%$ is reassuringly close to the value $Z_{\rm O} = 9\%$ from Paper I, considering that both values are probably uncertain by at least a factor of two.

The leading contender for IGM enrichment is outflows from starbursting dwarf galaxies (Heckman et al. 2001; Keeney et al. 2006). These starburst winds would be dominated by the products of the most massive stars, which show an elevated abundance of oxygen in relation to carbon as a result of α-process nucleosynthesis (Garnett et al. 1995; Sneden 2004). Within the large uncertainties, the observed $(C/O)_{\rm IGM} \approx (C/O)_\odot$ implies that the IGM is enriched by a more mature gas mixture from a broader range of stellar masses.

We can also directly compare measurements of O and C ions to determine $({\rm C/O})_{\rm IGM}$. Thirteen absorption systems show detections in both O VI and C III with $\langle N_{\rm CIII}/N_{\rm OVI} \rangle = 0.21^{+0.39}_{-0.14}$ (1σ uncertainty, Figure 11). We make some very crude assumptions for ionization fractions as discussed above, $f_{\rm CIII} = 0.8$ and $f_{\rm OVI} = 0.2$ based on peak CIE and/or photoionization values, and conclude that

$$\left(\frac{C}{O} \right)_{\rm IGM} = 0.1^{+0.2}_{-0.1} \left(\frac{C}{O} \right)_\odot \left(\frac{f_{\rm OVI}}{0.2} \right) \left(\frac{f_{\rm CIII}}{0.8} \right)^{-1}\ . \tag{15}$$

There are large uncertainties, but this sub-solar abundance ratio is more consistent with what we expect from an enrichment of the IGM by the most massive stars. However, it is in contradiction to the derived C/H and O/H metallicities from the multiphase plots discussed above and in Paper I.

Given that C III and O VI almost assuredly occupy different temperature phases in the IGM, as well as different spatial volumes within a given absorber (though they may share the same metallicity), these are not the best ions to use to investigate relative metallicities, so we view the $({\rm C/O})_{\rm IGM}$ ratio above with caution. Lithium-like C IV and N V are more useful probes of relative abundances with O VI. These data are available in STIS spectra and will be the subject of a future investigation.

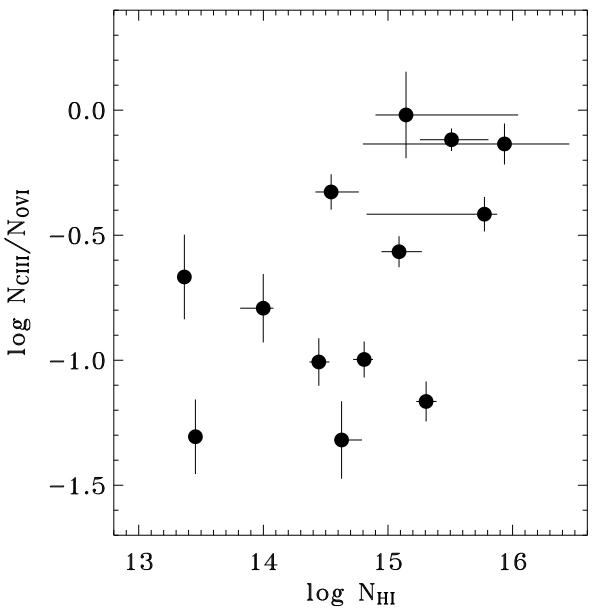

FIG. 11.— The C III/O VI multiphase ratio shows a weak correlation with $N_{\rm HI}$ at the 2σ level ($R \sim 0.6 \pm 0.2$). The mean $N_{\rm CIII}/N_{\rm OVI}$ is consistent with $(C/O) = 0.1^{+0.2}_{-0.1}\ (C/O)_\odot$.

5. CONCLUSIONS AND SUMMARY

We present *FUSE* observations of 31 AGN sight lines covering an integrated redshift path length of $\Delta z > 2$. We start with a known population of 171 Lyα absorbers with $W_{\rm Ly\alpha} > 80$ mÅ at $z \leq 0.3$ and measure corresponding absorption in higher Lyman lines. These allow us to determine $b_{\rm HI}$ and $N_{\rm HI}$ with a curve of growth, resulting in more accurate measurements than possible for Lyα-only analysis.

Higher Lyman lines are critical for accurate $N_{\rm HI}$ and $b_{\rm HI}$ measurements, particularly for stronger lines ($W_{\rm Ly\alpha} > 180$ mÅ) where Lyα absorption is saturated. We find that $N_{\rm Ly\alpha} < N_{\rm COG}$ for most cases and that $b_{\rm Ly\alpha}$ consistently overpredicts $b_{\rm COG}$, often by a factor of two or more (see also Shull et al. 2000).

We measure corresponding metal-line absorption in O VI (for $z \leq 0.15$) and C III ($z < 0.21$). In all, O VI is detected in 40 out of 129 possible absorbers, and C III is detected in 30 out of 148 absorbers. C III detection statistics give $d\mathcal{N}_{\rm CIII}/dz = 12^{+3}_{-2}$. We calculate a typical size for IGM absorbers from detection statistics in O VI and find $r_0 \sim 400$ kpc if absorbers are associated with $0.1L^*$ galaxies. This size is similar to the results of Tumlinson & Fang (2005) and consistent with constraints placed on r_0 from Hubble broadening and observed b-values.

Our observations strongly suggest that H I and C III probe photionized regions of the IGM, while O VI is primarily a product of collisional (shock) ionization and therefore a valid probe of the WHIM. Line width analysis sets an upper limit on absorber temperature. All three species have similar distributions of b-values, with median values $\sim$ 25 km s^{-1}. The O VI is consistent with WHIM-phase, collisionally ionized WHIM, but $\langle b({\rm HI})\rangle = 25 \pm 13$ km s^{-1} requires that the observed H I absorption arise in a medium with $T < 10^5$ K. Single-phase CLOUDY models featuring both photoionization and collisional ionization limit which areas of parameter space are allowed for O VI and C III absorbers. Observed $N_{\rm OVI}$ values require $\log U \gtrsim -2$, while observed $N_{\rm CIII}$ requires $\log U \lesssim -2$, regardless of temperature.

We calculate the column density distribution of H I absorbers and find that it follows a power law distribution $\mathcal{N}(N_{\rm HI}) \propto N_{\rm HI}^{-\beta}$ with $\beta = 1.68 \pm 0.11$, similar to the result found by Penton, Stocke, & Shull (2000, 2004). We find that C III absorbers also follow a power-law distribution with slope $\beta_{\rm CIII} = 1.68 \pm 0.04$, similar to $\beta_{\rm HI}$, but not as steep as $\beta_{\rm OVI} = 2.2 \pm 0.1$ found in Paper I. This similarity in N distribution slope is circumstantial evidence that H I and C III arise through similar mechanisms.

Our absorber sample includes 45 H I absorbers with good statistics in both O VI and C III lines. We interpret 12 absorbers with H I, O VI, and C III as multi-phase systems with shock-heated WHIM (probed by O VI) and a photoionized component seen in C III and H I. The four H I+C III systems are interpreted as unshocked, photoionized gas at 10^4 K. The eight systems with H I and O VI but no C III are probably multi-phase absorbers with photoionized H I and WHIM O VI. The 21 absorbers with neither O VI nor C III are most likely low-metallicity, unshocked systems. Stocke et al. (2005) find that these systems have larger nearest-neighbor distances than the population of metal absorbers.

Finally, the metallicity of IGM absorbers appears close to the canonical 10% solar value. The $N_{\rm HI}/N_{\rm CIII}$ multiphase relationship implies an IGM carbon metallicity $Z_C = 0.12\, Z_\odot\, (f_{\rm CIII}/0.8)^{-1}$, remarkably consistent with the result $Z_O = 0.09\, Z_\odot\, (f_{\rm OVI}/0.2)^{-1}$ from Paper I. This implies a near-solar abundance ratio of C/O in the IGM, higher than what we expect from stellar nucleosynthesis models which say that the IGM is preferentially enriched by O-rich massive stars.

Future work with other highly ionized species (e.g. C IV, Si III, and Si IV) will help constrain ionization and temperature and cast more light on the metallicity trends in the low-redshift universe. Deeper FUV observations will allow us to seach for lower column density absorbers, and additional sight lines from future observations will contribute redshift pathlength to the statistics.

It is our pleasure to acknowledge useful discussions with Nahum Arav, Jack Gabel, and Van Dixon. Steve Penton reduced the STIS/E140M data for six sight lines. We made extensive use of CLOUDY v.96.01 and are grateful to Gary Ferland and Peter van Hoof for technical assistance with the code. We would also like to thank Gerry Williger for a thorough job refereeing our manuscript. This work contains data obtained for the Guaranteed Time Team by the NASA-CNES-CSA *FUSE* mission operated by the Johns Hopkins University, as well as data from the *Hubble Space Telescope*. J.L.R. has received financial support from NSF grant AST-0302049. Financial support to the University of Colorado has been provided by NASA/*FUSE* contract NAS5-32985 and grant NAG5-13004, by our HST Lyα survey (GO Program 6593), and by theoretical grants from NASA/LTSA (NAG5-7262)and NSF (AST02-06042).

REFERENCES

Allende Prieto, C., Lambert, D. L., & Asplund, M. 2001, ApJ, 556, L63
Allende Prieto, C., Lambert, D. L., & Asplund, M. 2001, ApJ, 573, L137
Bechtold, J. B., Crotts, A. P. S., Duncan, R. C., & Fang, Y. 1994, ApJ, 437, L83
Bechtold, J. B., et al. 2002, ApJS, 140, 143
Blanton, M. R., et al. 2003, ApJ, 592, 819
Birnboim, Y. & Dekel, A. 2002, MNRAS, 345, 349
Cen, R., & Ostriker, J. P. 1999a, ApJ, 519, L109
Cen, R., & Ostriker, J. P. 1999b, ApJ, 514, 1
Cen, R., Tripp, T. M., Ostriker, J. P., & Jenkins, E. 2001, ApJ, 559, L5
Chen, X., Weinberg, D. H., Katz, N., & Davé, R. 2003, ApJ, 594, 42
Collins, J. A., Shull, J. M., & Giroux, M. L. 2004, ApJ, 605, 216
Crenshaw, D. M., Kraemer, S. B., Boggess, A., Maran, S. P., Mushotzky, R. F., & Wu, C. 1999, ApJ, 516, 750
Danforth, C. W. & Shull, J. M. 2005, ApJ, 624, 555 (Paper I)
Davé, R., et al. 1999, ApJ, 511, 521
Davé, R., et al. 2001, ApJ, 552, 473
Davé, R., & Tripp, T. M. 2001, ApJ, 553, 528
Dinshaw, N., Weymann, R. J., Impey, C. D., Foltz, C. B., Morris, S. L., & Ake, T. 1997, ApJ, 437, L87
Donahue, M. & Shull, J. M. 1991, ApJ, 383, 511
Ferland, G. J., et al. 1998, PASP, 110, 761
Furlanetto, S. R., Phillips, L. A., & Kamionkowski, M. 2005, MNRAS, 359, 295
Garnett, D. R., et al. 1995, ApJ, 443, 64
Gehrels, N. 1986, ApJ, 303, 336
Gillmon, K., Shull, J. M., Tumlinson, J., & Danforth, C. W. 2005, ApJ, submitted (astro-ph/0507581)
Hartigan, P., Raymond, J., & Hartmann, L. 1987, ApJ, 316, 323
Hebrard, G., et al. 2006, ApJ, accepted (astro-ph/0508611)
Heckman, T. M., et al. 2001, ApJ, 554, 1021
Heckman, T. M., Norman, C. A., Strickland, D. K., & Sembach, K. R. 2002, ApJ, 577, 691
Hu, E. M., Kim, T.-S., Cowie, L. L., Songaila, A., & Rauch, M. 1995, AJ, 110, 1526
Jenkins, E. B. 1986, ApJ, 304, 739
Jenkins, E. B., et al. 2003, AJ, 125, 2824
Keeney, B., Danforth, C. W., Stocke, J. T., Penton, S. V., & Shull, J. M. 2006, in prep
Kim, T.-S., Hu, E. M., Cowie, L. L., & Songaila, A. 1997, AJ, 114, 1
Kriss, G. A. 2002, in "Mass Outflow in Active Galactic Nuclei: New Perspectives", ASP Conf. Ser. 255, 69
Korista, K., et al. 1997, ApJS, 108, 401

Lopez, S., Reimers, D., Rauch, M., Sargent, W. L., & Smette, A. 1999, ApJ, 513, 598
Lu, L., Sargent, W. L. W., Womble, D. S., & Takada-Hidai, M. 1996, ApJ, 472, 509
Mathews, W. D., & Ferland, G. 1987, ApJ, 323, 456
Moos, H. W., et al. 2000, ApJ, 538, L1
Parnell, H. C. & Carswell, R. F. 1988, MNRAS, 230, 491
Penton, S. V., Stocke, J. T., & Shull, J. M. 2000, ApJS, 130, 121
Penton, S. V., Shull, J. M., & Stocke, J. T. 2000, ApJ, 544, 150
Penton, S. V., Stocke, J. T., & Shull, J. M. 2003, ApJ, 565, 720
Penton, S. V., Stocke, J. T., & Shull, J. M. 2004, ApJS, 152, 29
Prochaska, J. X., Chen, H-W, Howk, J. C., Weiner, B. J., & Mulchaey, J. 2004, ApJ, 617, 718
Rajan, N. & Shull, J. M. 2005, in prep.
Richter, P., Savage, B. D., Tripp, T. M., & Sembach, K. R. 2004, ApJS, 153, 165
Richter, P., Savage, B. D., Tripp, T. M., & Sembach, K. R. 2005, Proceedings of Science, "Baryons in Dark Matter Halos", Novigrad, Croatia (astro-ph/0412133)
Sahnow, D. J., et al. 2000, ApJ, 538, L7
Savage, B. D., & Sembach, K. R. 1991, ApJ, 379, 245
Savage, B. D., Sembach, K. R., Tripp, T. M., & Richter, P. 2002, ApJ, 564, 631
Schaye, J. 2001, ApJ, 559, 507
Sembach, K. R., Howk, J. C., Savage, B. D., Shull, J. M., & Oegerle, W. R. 2001, ApJ, 561, 573
Sembach, K. R., Tripp, T. M., Savage, B. D., & Richter, P. 2004, ApJS, 153, 165
Shull, J. M., et al. 1998, AJ, 116 2094
Shull, J. M., Roberts, D., Giroux, M. L., Penton, S. V., & Fardal, M. A. 1999, ApJ, 118, 1450
Shull, J. M., et al. 2000, ApJ, 538, L13
Shull, J. M., Stocke, J. T., & Penton, S. V. 1996, AJ, 111, 72
Shull, J. M., Tumlinson, J., & Giroux, M. 2003, ApJ, 594, L107
Sneden, C. 2004, Mem. S. A. It., 75, 267
Stocke, J. T., Shull, J. M., & Penton, S. V. 2005, in "From Planets to Cosmology: Proceedings of STScI May 2004 Symposium", in press (astro-ph/0407352)
Stocke, J. T., Penton, S. V., Danforth, C. W., Shull, J. M., Tumlinson, J., & McLin, K. 2005, ApJ, submitted
Sutherland, R. S., & Dopita, M. A. 1993, ApJS, 88, 253
Tripp, T. M., Lu, L., & Savage, B. D. 1998, ApJ, 508, 200
Tripp, T. M., Savage, B. D., & Jenkins, E. B. 2000, ApJ, 534, L1
Tumlinson, J., Shull, J. M., Giroux, M. L., & Stocke, J. T. 2005, ApJ, 620, 95
Tumlinson, J. & Fang, T. 2005, ApJ, 623, L97
Weinberg, D. H., Katz, N., & Hernquist, L. 1998, in ASP Conf. Ser. 148, Origins, ed. C. E. Woodward, J. M. Shull, & H. A. Thronson (San Francisco,: ASP), 21
Weymann, R., et al. 1998, ApJ, 506, 1
Williger, G. M., et al. 2005, ApJ, 625, 210
Williger, G. M., et al. ApJ, in press, 10 Jan. 2006 (astro-ph/0505586)
Young, P. A., Impey, C. D., & Foltz, C. B. 2001, ApJ, 549, 76

TABLE 2
Lyα Absorbers

Sight Line	Abs #	$z_{\rm abs}$	$v_{\rm lsr}$ (km/s)	b (km/s)	$W_{\rm rest}$ (mÅ)	Source and Notes
Mrk335	1	0.00655	1965 ± 6	75 ± 7	229 ± 30	Penton, Stocke, & Shull (2000)
Mrk335	2	0.00765	2295 ± 12	73 ± 17	81 ± 26	Penton, Stocke, & Shull (2000)
Mrk335	3	0.02090	6269 ± 6	75 ± 6	130 ± 14	Penton, Stocke, & Shull (2000)
IZw1	1	0.00539	1617 ± 5	···	120 ± 37	Shull, Stocke, & Penton (1996)
IZw1	2	0.00954	2861 ± 9	···	84 ± 40	Shull, Stocke, & Penton (1996)
IZw1	3	0.01710	5130 ± 12	···	84 ± 47	Shull, Stocke, & Penton (1996)
TonS180	1	0.01834	5502 ± 11	51 ± 5	268 ± 54	Penton, Stocke, & Shull (2004)
TonS180	2	0.02339	7017 ± 11	56 ± 4	222 ± 29	Penton, Stocke, & Shull (2004)
TonS180	3	0.04304	12912 ± 12	81 ± 15	107 ± 39	Penton, Stocke, & Shull (2004)
TonS180	4	0.04356	13068 ± 12	52 ± 5	140 ± 27	Penton, Stocke, & Shull (2004)
TonS180	5	0.04505	13515 ± 12	58 ± 7	140 ± 29	Penton, Stocke, & Shull (2004)
TonS180	6	0.04560	13681 ± 11	54 ± 4	212 ± 29	Penton, Stocke, & Shull (2004)
Fairall9	1	0.03162	9487 ± 6	43 ± 6	84 ± 13	Penton, Stocke, & Shull (2000)
HE0226-4110	1	0.02938	8815 ± 2	33 ± 3	189 ± 5	this work, blend
HE0226-4110	2	0.04606	13817 ± 1	25 ± 2	163 ± 5	this work
HE0226-4110	4	0.16328	48983 ± 1	39 ± 1	483 ± 1	this work
HE0226-4110	5	0.19378	58134 ± 7	40 ± 1	187 ± 1	this work
HE0226-4110	6	0.19846	59537 ± 1	38 ± 2	352 ± 10	this work
HE0226-4110	7	0.20688	62064 ± 1	33 ± 2	549 ± 31	this work
HE0226-4110	8	0.21988	65965 ± 1	29 ± 1	347 ± 14	this work
HE0226-4110	9	0.24498	73493 ± 1	34 ± 1	350 ± 10	this work
HE0226-4110	10	0.27130	81390 ± 1	40 ± 1	296 ± 1	this work
HE0226-4110	11	0.27939	83818 ± 6	38 ± 6	137 ± 4	this work
HE0226-4110	12	0.29111	87333 ± 5	29 ± 5	143 ± 6	this work
PKS0405-123	1	0.02996	8989 ± 1	30 ± 2	319 ± 7	this work
PKS0405-123	3	0.09183	27549 ± 0	38 ± 1	470 ± 5	this work
PKS0405-123	4	0.09657	28970 ± 1	46 ± 1	494 ± 18	this work
PKS0405-123	7	0.13095	39285 ± 5	42 ± 7	84 ± 5	this work
PKS0405-123	8	0.13228	39683 ± 0	20 ± 1	139 ± 5	this work
PKS0405-123	9	0.16703	50109 ± 4	63 ± 4	178 ± 5	this work
PKS0405-123	10	0.18270	54809 ± 1	37 ± 0	751 ± 46	this work
Akn120	1	0.02653	7960 ± 5	27 ± 4	147 ± 22	Penton, Stocke, & Shull (2000)
VIIZw118	1	0.00820	2460 ± 6	44 ± 4	267 ± 35	Penton, Stocke, & Shull (2004)
PG0804+761	1	0.00382	1147 ± 11	38 ± 4	165 ± 29	Penton, Stocke, & Shull (2004)
PG0804+761	2	0.01851	5552 ± 11	50 ± 4	324 ± 44	Penton, Stocke, & Shull (2004)
PG0953+415	1	0.01602	4806 ± 0	···	162 ± 13	Savage et al. (2002)
PG0953+415	2	0.01655	4965 ± 0	···	123 ± 12	Savage et al. (2002)
PG0953+415	3	0.05876	17628 ± 0	···	280 ± 14	Savage et al. (2002)
PG0953+415	4	0.06807	20421 ± 0	···	290 ± 13	Savage et al. (2002)
PG0953+415	5	0.09315	27945 ± 0	···	174 ± 13	Savage et al. (2002)
PG0953+415	6	0.10939	32817 ± 0	···	168 ± 11	Savage et al. (2002)
PG0953+415	7	0.11558	34674 ± 0	···	115 ± 12	Savage et al. (2002)
PG0953+415	8	0.11826	35478 ± 0	···	179 ± 10	Savage et al. (2002)
PG0953+415	9	0.12801	38403 ± 0	···	94 ± 10	Savage et al. (2002)
PG0953+415	18	0.14246	42739 ± 0	···	141 ± 23	this work

TABLE 2 — *Continued*

Sight Line	Abs #	$z_{\rm abs}$	$v_{\rm lsr}$ (km/s)	b (km/s)	$W_{\rm rest}$ (mÅ)	Source and Notes
PG0953+415	19	0.14258	42774 ± 0	···	114 ± 23	this work
PG0953+415	11	0.17984	53952 ± 0	···	84 ± 11	Savage et al. (2002)
PG0953+415	12	0.19142	57426 ± 0	···	177 ± 15	Savage et al. (2002)
PG0953+415	13	0.19221	57663 ± 0	···	122 ± 18	Savage et al. (2002)
PG0953+415	14	0.19360	58080 ± 0	···	269 ± 15	Savage et al. (2002)
Mrk421	1	0.01012	3035 ± 6	35 ± 5	86 ± 15	Penton, Stocke, & Shull (2000)
PG1116+215	1	0.00500	1499 ± 9	52 ± 12	82 ± 33	Penton, Stocke, & Shull (2004)
PG1116+215	2	0.01638	4913 ± 8	30 ± 9	90 ± 32	Penton, Stocke, & Shull (2004)
PG1116+215	4	0.02839	8518 ± 8	45 ± 4	227 ± 32	Penton, Stocke, & Shull (2004)
PG1116+215	5	0.03235	9705 ± 0	···	92 ± 16	Tripp, Lu, & Savage (1998)
PG1116+215	6	0.04119	12357 ± 30	89 ± 39	88 ± 82	Penton, Stocke, & Shull (2004)
PG1116+215	7	0.05899	17698 ± 7	51 ± 6	167 ± 31	Penton, Stocke, & Shull (2004)
PG1116+215	8	0.08123	24369 ± 0	···	110 ± 17	Tripp, Lu, & Savage (1998)
PG1116+215	9	0.11912	35735 ± 0	···	117 ± 22	Tripp, Lu, & Savage (1998)
PG1116+215	10	0.13860	41579 ± 0	···	476 ± 28	Tripp, Lu, & Savage (1998), two components
PG1116+215	11	0.16625	49876 ± 0	···	741 ± 20	Tripp, Lu, & Savage (1998), three components
PG1116+215	12	0.17368	52104 ± 0	···	262 ± 12	Tripp, Lu, & Savage (1998), probably intrinsic
PG1211+143	1	0.00710	2130 ± 18	97 ± 3	186 ± 19	Penton, Stocke, & Shull (2004)
PG1211+143	2	0.01648	4944 ± 17	58 ± 7	189 ± 46	Penton, Stocke, & Shull (2004)
PG1211+143	3	0.01679	5036 ± 17	34 ± 6	154 ± 40	Penton, Stocke, & Shull (2004)
PG1211+143	4	0.02205	6615 ± 18	32 ± 13	89 ± 54	Penton, Stocke, & Shull (2004)
PG1211+143	5	0.02334	7002 ± 17	54 ± 6	150 ± 30	Penton, Stocke, & Shull (2004)
PG1211+143	6	0.02584	7752 ± 17	75 ± 6	159 ± 26	Penton, Stocke, & Shull (2004)
PG1211+143	7	0.04337	13010 ± 17	54 ± 8	216 ± 56	Penton, Stocke, & Shull (2004)
PG1211+143	8	0.04356	13068 ± 17	31 ± 7	95 ± 30	Penton, Stocke, & Shull (2004)
PG1211+143	14	0.05128	15384 ± 90	···	999 ± 60	two components
PG1211+143	11	0.05202	15605 ± 17	42 ± 5	132 ± 28	Penton, Stocke, & Shull (2004)
PG1211+143	12	0.06443	19328 ± 18	74 ± 3	564 ± 31	Penton, Stocke, & Shull (2004)
PG1211+143	13	0.06489	19468 ± 18	56 ± 3	249 ± 26	Penton, Stocke, & Shull (2004)
3C273	1	0.00338	1015 ± 6	69 ± 5	369 ± 36	Penton, Stocke, & Shull (2000)
3C273	2	0.00529	1586 ± 6	72 ± 4	373 ± 30	Penton, Stocke, & Shull (2000)
3C273	3	0.02944	8832 ± 8	61 ± 10	114 ± 25	Penton, Stocke, & Shull (2000)
3C273	4	0.04897	14691 ± 7	61 ± 8	140 ± 25	Penton, Stocke, & Shull (2000)
3C273	5	0.06652	19956 ± 6	62 ± 4	297 ± 25	Penton, Stocke, & Shull (2000)
3C273	6	0.09012	27036 ± 0	···	160 ± 20	Sembach et al. (2001)
3C273	7	0.12007	36021 ± 0	···	138 ± 11	Sembach et al. (2001)
3C273	8	0.14660	43980 ± 0	···	355 ± 20	Sembach et al. (2001)
PG1259+593	1	0.00229	687 ± 9	42 ± 4	190 ± 24	Sembach et al. (2004)
PG1259+593	2	0.00760	2280 ± 6	35 ± 2	301 ± 15	Sembach et al. (2004)
PG1259+593	3	0.02217	6651 ± 6	30 ± 2	160 ± 9	Sembach et al. (2004)
PG1259+593	5	0.04606	13818 ± 9	···	878 ± 29	Sembach et al. (2004)
PG1259+593	6	0.04650	13950 ± 0	89 ± 15	463 ± 118	this work
PG1259+593	7	0.05376	16127 ± 1	25 ± 2	99 ± 5	this work
PG1259+593	8	0.06644	19932 ± 6	29 ± 3	162 ± 12	Sembach et al. (2004)
PG1259+593	9	0.06931	20793 ± 5	47 ± 7	97 ± 5	this work
PG1259+593	10	0.08933	26799 ± 6	29 ± 2	273 ± 11	Sembach et al. (2004)
PG1259+593	11	0.12388	37165 ± 2	27 ± 3	132 ± 8	this work
PG1259+593	12	0.14852	44556 ± 9	42 ± 2	254 ± 9	Sembach et al. (2004)
PG1259+593	13	0.15050	45150 ± 5	60 ± 7	184 ± 5	this work, blend
PG1259+593	14	0.19620	58860 ± 9	33 ± 3	201 ± 14	Sembach et al. (2004)
PG1259+593	15	0.21949	65847 ± 9	31 ± 4	552 ± 26	Sembach et al. (2004)
PG1259+593	16	0.22313	66939 ± 6	35 ± 1	247 ± 8	Sembach et al. (2004)
PG1259+593	17	0.22471	67413 ± 9	29 ± 2	169 ± 12	Sembach et al. (2004)
PG1259+593	18	0.25642	76926 ± 6	25 ± 1	184 ± 6	Sembach et al. (2004)
PG1259+593	19	0.25971	77913 ± 9	41 ± 5	249 ± 10	Sembach et al. (2004)
PG1259+593	20	0.28335	85005 ± 9	37 ± 5	158 ± 9	Sembach et al. (2004)
PG1259+593	21	0.29236	87708 ± 9	24 ± 3	404 ± 19	Sembach et al. (2004)
PKS1302-102	1	0.00437	1311 ± 0	16 ± 0	293 ± 0	this work
PKS1302-102	3	0.04226	12679 ± 1	36 ± 2	417 ± 8	this work
PKS1302-102	4	0.04446	13339 ± 1	31 ± 2	145 ± 5	this work
PKS1302-102	5	0.04613	13839 ± 4	46 ± 6	108 ± 5	this work
PKS1302-102	6	0.04658	13974 ± 2	48 ± 3	232 ± 5	this work
PKS1302-102	7	0.05967	17902 ± 2	24 ± 3	87 ± 5	this work
PKS1302-102	8	0.06473	19420 ± 1	37 ± 1	249 ± 5	this work
PKS1302-102	9	0.08655	25965 ± 1	22 ± 1	113 ± 5	this work
PKS1302-102	10	0.09398	28193 ± 1	34 ± 2	422 ± 5	this work
PKS1302-102	21	0.09483	28450 ± 30	···	881 ± 167	this work, two components
PKS1302-102	13	0.09889	29668 ± 2	49 ± 1	504 ± 9	this work
PKS1302-102	14	0.12336	37009 ± 2	27 ± 3	110 ± 5	this work
PKS1302-102	15	0.14532	43596 ± 1	65 ± 2	893 ± 19	this work
PKS1302-102	16	0.19160	57479 ± 0	23 ± 0	335 ± 4	this work
PKS1302-102	17	0.22454	67362 ± 2	30 ± 0	267 ± 23	this work
PKS1302-102	18	0.22555	67665 ± 2	39 ± 0	281 ± 8	this work
PKS1302-102	19	0.24877	74630 ± 1	19 ± 0	210 ± 2	this work
PKS1302-102	20	0.25211	75633 ± 2	33 ± 0	365 ± 5	this work

TABLE 2 — *Continued*

Sight Line	Abs #	$z_{\rm abs}$	$v_{\rm lsr}$ (km/s)	b (km/s)	$W_{\rm rest}$ (mÅ)	Source and Notes
Mrk1383	1	0.02830	8490 ± 8	65 ± 5	218 ± 30	Penton, Stocke, & Shull (2004)
Mrk1383	2	0.05189	15566 ± 8	46 ± 3	282 ± 20	Penton, Stocke, & Shull (2004)
Mrk817	1	0.00699	2097 ± 5	40 ± 4	135 ± 15	Penton, Stocke, & Shull (2000)
Mrk478	1	0.00527	1582 ± 10	45 ± 4	194 ± 31	Penton, Stocke, & Shull (2004)
Mrk478	2	0.02929	8788 ± 10	58 ± 3	290 ± 30	Penton, Stocke, & Shull (2004)
Mrk478	3	0.06531	19593 ± 10	43 ± 6	84 ± 18	Penton, Stocke, & Shull (2004)
Mrk876	1	0.00319	958 ± 0	72 ± 8	324 ± 52	Shull et al. (2000)
Mrk876	2	0.01162	3486 ± 0	46 ± 0	236 ± 50	this work
H1821+643	1	0.02447	7342 ± 5	47 ± 3	298 ± 20	Penton, Stocke, & Shull (2000)
H1821+643	2	0.05688	17064 ± 0	···	87 ± 14	Tripp, Lu, & Savage (1998)
H1821+643	3	0.06722	20166 ± 0	···	159 ± 13	Tripp, Lu, & Savage (1998)
H1821+643	4	0.11968	35903 ± 0	···	101 ± 8	Tripp, Lu, & Savage (1998)
H1821+643	5	0.12131	36394 ± 0	···	390 ± 0	Tripp, Lu, & Savage (1998)
H1821+643	6	0.14758	44274 ± 0	···	229 ± 14	Tripp, Lu, & Savage (1998)
H1821+643	7	0.16990	50969 ± 0	···	523 ± 17	Tripp, Lu, & Savage (1998)
H1821+643	10	0.21170	63510 ± 0	···	103 ± 14	Tripp, Lu, & Savage (1998)
H1821+643	11	0.21311	63933 ± 0	49 ± 2	483 ± 18	Shull et al. (2000)
H1821+643	12	0.21601	64803 ± 0	···	145 ± 14	Tripp, Lu, & Savage (1998)
H1821+643	13	0.22473	67420 ± 0	87 ± 2	417 ± 17	Shull et al. (2000), double profile
H1821+643	14	0.22612	67836 ± 0	···	279 ± 20	Tripp, Lu, & Savage (1998)
H1821+643	15	0.22637	67911 ± 0	···	168 ± 15	Tripp, Savage, & Jenkins (2000)
H1821+643	19	0.25836	77507 ± 0	···	114 ± 33	Tripp, Lu, & Savage (1998)
H1821+643	20	0.26133	78398 ± 0	···	181 ± 34	Tripp, Lu, & Savage (1998)
H1821+643	21	0.26659	79977 ± 0	···	177 ± 12	Tripp, Savage, & Jenkins (2000)
PKS2005-489	1	0.01649	4947 ± 13	59 ± 3	299 ± 26	Penton, Stocke, & Shull (2004)
PKS2005-489	2	0.01687	5061 ± 12	40 ± 3	281 ± 21	Penton, Stocke, & Shull (2004)
PKS2005-489	3	0.05769	17306 ± 13	47 ± 3	294 ± 15	Penton, Stocke, & Shull (2004)
PKS2005-489	4	0.06493	19478 ± 13	37 ± 3	249 ± 15	Penton, Stocke, & Shull (2004)
Mrk509	1	0.00853	2560 ± 6	40 ± 5	209 ± 32	Penton, Stocke, & Shull (2000)
IIZw136	1	0.02773	8320 ± 7	33 ± 4	192 ± 22	Penton, Stocke, & Shull (2004)
PHL1811	1	0.01179	3537 ± 7	45 ± 9	360 ± 32	this work, Jenkins et al. (2003)
PHL1811	2	0.01734	5201 ± 3	24 ± 5	236 ± 29	this work, Jenkins et al. (2003)
PHL1811	3	0.05006	15017 ± 19	57 ± 26	123 ± 4	this work, Jenkins et al. (2003), maybe double?
PHL1811	4	0.05142	15426 ± 11	62 ± 15	248 ± 11	this work
PHL1811	5	0.07340	22020 ± 3	29 ± 7	447 ± 96	this work, Jenkins et al. (2003)
PHL1811	6	0.07770	23311 ± 2	26 ± 6	410 ± 77	this work, Jenkins et al. (2003)
PHL1811	7	0.07896	23688 ± 2	24 ± 8	497 ± 141	this work, Jenkins et al. (2003)
PHL1811	8	0.08072	24215 ± 0	51 ± 7	841 ± 106	this work, Jenkins et al. (2003), Lyman limit system
PHL1811	9	0.13221	39664 ± 3	35 ± 5	430 ± 45	this work, Jenkins et al. (2003)
PHL1811	10	0.13535	40606 ± 3	25 ± 5	267 ± 29	this work, Jenkins et al. (2003)
PHL1811	11	0.17640	52919 ± 4	35 ± 7	445 ± 68	this work, Jenkins et al. (2003)
PHL1811	12	0.18084	54251 ± 7	26 ± 8	91 ± 4	this work
PKS2155-304	1	0.01671	5013 ± 7	58 ± 11	82 ± 22	Penton, Stocke, & Shull (2000)
PKS2155-304	2	0.01706	5119 ± 7	80 ± 5	218 ± 20	Penton, Stocke, & Shull (2000)
PKS2155-304	3	0.04530	13591 ± 6	39 ± 6	101 ± 18	Penton, Stocke, & Shull (2000)
PKS2155-304	4	0.05395	16185 ± 5	58 ± 3	331 ± 12	Shull, Tumlinson, & Giroux (2003)
PKS2155-304	5	0.05658	16974 ± 5	63 ± 6	495 ± 10	Shull, Tumlinson, & Giroux (2003)
PKS2155-304	6	0.05716	17147 ± 5	87 ± 11	353 ± 8	Shull, Tumlinson, & Giroux (2003)
PKS2155-304	7	0.05904	17713 ± 6	35 ± 5	139 ± 21	Penton, Stocke, & Shull (2000)
PKS2155-304	8	0.06024	18073 ± 7	47 ± 8	99 ± 20	Penton, Stocke, & Shull (2000)
MR2251-178	1	0.01068	3205 ± 10	69 ± 4	349 ± 37	Penton, Stocke, & Shull (2004)
MR2251-178	2	0.03245	9735 ± 10	43 ± 3	181 ± 23	Penton, Stocke, & Shull (2004)

TABLE 3
H I Absorber Measurements

Target	Abs#	$z_{\rm abs}$	$cz_{\rm abs}$	$b_{\rm HI}$	$\log N_{\rm HI}$	notes[a]
Mrk335	1	0.0066	1965	> 43	$13.611^{+0.062}_{-0.020}$	this work
Mrk335	2	0.0077	2295	$17^{+\infty}_{-13}$	$13.295^{+0.341}_{-0.269}$	this work
Mrk335	3	0.0209	6269	$25^{+\infty}_{-14}$	$13.518^{+0.200}_{-0.149}$	this work
IZw1	1	0.0054	1617	20 ± 10	$13.500^{+0.292}_{-0.062}$	$W_{\rm Ly\alpha}$ [b]
IZw1	2	0.0095	2861	20 ± 10	$13.289^{+0.137}_{-0.039}$	$W_{\rm Ly\alpha}$ [b]
IZw1	3	0.0171	5130	20 ± 10	$13.289^{+0.137}_{-0.039}$	$W_{\rm Ly\alpha}$ [b]
TonS180	1	0.0183	5502	$30^{+\infty}_{-12}$	$13.992^{+0.178}_{-0.143}$	this work
TonS180	2	0.0234	7017	16^{+6}_{-5}	$14.385^{+0.522}_{-0.234}$	this work
TonS180	3	0.0430	12912	$10^{+\infty}_{-5}$	$13.763^{+0.510}_{-0.386}$	this work
TonS180	4	0.0436	13068	11^{+8}_{-4}	$14.082^{+0.463}_{-0.301}$	this work
TonS180	5	0.0450	13515	$17^{+\infty}_{-7}$	$13.662^{+0.034}_{-0.323}$	this work
TonS180	6	0.0456	13681	20^{+20}_{-5}	$13.999^{+0.082}_{-0.185}$	this work
HE0226-4110	1	0.0294	8815	15^{+4}_{-2}	$14.204^{+0.202}_{-0.241}$	this work
HE0226-4110	2	0.0461	13817	13^{+5}_{-2}	$14.089^{+0.161}_{-0.270}$	this work
HE0226-4110	4	0.1633	48983	34^{+7}_{-4}	$14.815^{+0.328}_{-0.286}$	this work
HE0226-4110	5	0.1938	58134	$14^{+\infty}_{-0}$	$14.220^{+0.000}_{-0.621}$	this work
HE0226-4110	6	0.1985	59537	30^{+31}_{-6}	$14.329^{+0.318}_{-0.338}$	this work
HE0226-4110	7	0.2069	62064	31^{+5}_{-4}	$15.506^{+0.300}_{-0.236}$	this work
HE0226-4110	8	0.2199	65965	24^{+3}_{-2}	$14.655^{+0.056}_{-0.138}$	this work
HE0226-4110	9	0.2450	73493	22 ± 2	$14.856^{+0.235}_{-0.131}$	this work
HE0226-4110	10	0.2713	81390	32 ± 1	$13.750^{+0.500}_{-0.500}$	Lyα fit, this work
HE0226-4110	11	0.2794	83818	30 ± 5	$13.280^{+0.500}_{-0.500}$	Lyα fit, this work
HE0226-4110	12	0.2911	87333	23 ± -4	$13.320^{+0.500}_{-0.500}$	Lyα fit, this work
PKS0405-123	1	0.0300	8989	30^{+5}_{-3}	$14.202^{+0.073}_{-0.083}$	this work
PKS0405-123	3	0.0918	27549	37 ± 3	$14.554^{+0.106}_{-0.054}$	this work, [c,d]
PKS0405-123	4	0.0966	28970	37 ± 3	$14.695^{+0.099}_{-0.072}$	this work
PKS0405-123	7	0.1310	39285	43 ± 7	$13.252^{+0.060}_{-0.060}$	Lyα fit, this work
PKS0405-123	8	0.1323	39683	17^{+58}_{-5}	$13.672^{+0.177}_{-0.213}$	this work
PKS0405-123	9	0.1670	50109	44^{+32}_{-15}	$15.987^{+0.425}_{-0.264}$	this work
PKS0405-123	10	0.1827	54809	57^{+14}_{-7}	$14.833^{+0.073}_{-0.206}$	this work, [d]
Akn120	1	0.0265	7960	$23^{+\infty}_{-15}$	$13.602^{+0.796}_{-0.205}$	this work
VIIZw118	1	0.0082	2460	23^{+10}_{-6}	$14.191^{+0.161}_{-0.119}$	this work
PG0804+761	1	0.0038	1147	14^{+5}_{-4}	$14.057^{+0.199}_{-0.109}$	this work
PG0804+761	2	0.0185	5552	33^{+15}_{-9}	$14.128^{+0.068}_{-0.067}$	this work
PG0953+415	1	0.0160	4806	15^{+10}_{-3}	$13.889^{+0.163}_{-0.173}$	this work
PG0953+415	2	0.0166	4965	$14^{+\infty}_{-5}$	$13.635^{+0.220}_{-0.267}$	this work
PG0953+415	3	0.0588	17628	27^{+16}_{-5}	$14.107^{+0.125}_{-0.181}$	this work
PG0953+415	4	0.0681	20421	22 ± 2	$14.445^{+0.085}_{-0.075}$	this work
PG0953+415	5	0.0931	27945	$41^{+\infty}_{-23}$	$13.612^{+0.160}_{-0.091}$	this work
PG0953+415	6	0.1094	32817	19^{+24}_{-5}	$13.774^{+0.139}_{-0.148}$	this work
PG0953+415	7	0.1156	34674	10^{+4}_{-2}	$13.880^{+0.186}_{-0.158}$	this work
PG0953+415	8	0.1183	35478	$48^{+\infty}_{-28}$	$13.606^{+0.149}_{-0.063}$	this work
PG0953+415	9	0.1280	38403	10^{+55}_{-3}	$13.560^{+0.222}_{-0.244}$	this work
PG0953+415	11	0.1798	53952	$7^{+\infty}_{-1}$	$13.778^{+0.013}_{-0.634}$	this work
PG0953+415	12	0.1914	57426	14^{+5}_{-2}	$14.132^{+0.029}_{-0.189}$	this work
PG0953+415	13	0.1922	57663	9^{+5}_{-2}	$14.002^{+0.186}_{-0.252}$	this work
PG0953+415	14	0.1936	58080	26^{+17}_{-5}	$14.091^{+0.145}_{-0.180}$	this work
PG0953+415	18	0.1425	42739	29 ± 2	$13.455^{+0.032}_{-0.032}$	Lyα fit, this work
PG0953+415	19	0.1426	42774	33 ± 3	$13.366^{+0.038}_{-0.038}$	Lyα fit, this work
Mrk421	1	0.0101	3035	$5^{+\infty}_{-1}$	$14.305^{+0.037}_{-1.170}$	this work
PG1116+215	1	0.0050	1499	$18^{+\infty}_{-13}$	$13.292^{+0.074}_{-0.317}$	this work
PG1116+215	2	0.0164	4913	7 ± 4	$13.917^{+0.681}_{-0.089}$	this work
PG1116+215	4	0.0284	8518	$41^{+\infty}_{-21}$	$13.772^{+0.132}_{-0.121}$	this work
PG1116+215	5	0.0323	9705	$37^{+\infty}_{-24}$	$13.286^{+0.019}_{-0.120}$	this work
PG1116+215	6	0.0412	12357	89 ± 39	$13.290^{+0.030}_{-0.010}$	Penton et al. (2004)
PG1116+215	7	0.0590	17698	$19^{+\infty}_{-6}$	$13.782^{+0.005}_{-0.334}$	this work
PG1116+215	8	0.0812	24369	10^{+6}_{-3}	$13.783^{+0.189}_{-0.150}$	this work
PG1116+215	9	0.1191	35735	12^{+22}_{-5}	$13.677^{+0.187}_{-0.163}$	this work
PG1116+215	10	0.1386	41579	23^{+13}_{-4}	$15.935^{+0.521}_{-1.136}$	this work

TABLE 3 — *Continued*

Target	Abs#	$z_{\rm abs}$	$cz_{\rm abs}$	$b_{\rm HI}$	$\log N_{\rm HI}$	notes[a]
PG1116+215	11	0.1663	49876	$57^{+\infty}_{-5}$	$14.796^{+0.104}_{-0.259}$	this work
PG1116+215	12	0.1737	52104	18^{+4}_{-1}	$14.640^{+0.069}_{-0.279}$	this work
PG1211+143	1	0.0071	2130	15^{+5}_{-3}	$14.124^{+0.221}_{-0.172}$	this work
PG1211+143	2	0.0165	4944	$37^{+\infty}_{-25}$	$13.670^{+0.288}_{-0.211}$	this work
PG1211+143	3	0.0168	5036	14^{+24}_{-6}	$13.934^{+0.400}_{-0.249}$	this work
PG1211+143	4	0.0221	6615	32 ± 13	$13.300^{+0.030}_{-0.010}$	Penton et al. (2004)
PG1211+143	5	0.0233	7002	17^{+44}_{-7}	$13.733^{+0.139}_{-0.144}$	this work
PG1211+143	6	0.0258	7752	> 15	$13.417^{+0.281}_{-0.010}$	this work
PG1211+143	7	0.0434	13010	$28^{+\infty}_{-14}$	$13.840^{+0.158}_{-0.125}$	this work
PG1211+143	8	0.0436	13068	31 ± 7	$13.320^{+0.500}_{-0.500}$	Penton et al. (2004)
PG1211+143	14	0.0513	15384	$55^{+\infty}_{-5}$	$15.774^{+0.102}_{-0.946}$	this work
PG1211+143	11	0.0520	15605	$18^{+\infty}_{-9}$	$13.604^{+0.177}_{-0.186}$	this work
PG1211+143	12	0.0644	19328	36^{+4}_{-5}	$15.089^{+0.183}_{-0.141}$	this work
PG1211+143	13	0.0649	19468	20^{+12}_{-4}	$14.292^{+0.187}_{-0.292}$	this work
3C273	1	0.0034	1015	37^{+12}_{-7}	$14.186^{+0.042}_{-0.052}$	this work, [d]
3C273	2	0.0053	1586	19^{+7}_{-4}	$15.666^{+0.626}_{-0.756}$	this work
3C273	3	0.0294	8832	10^{+7}_{-3}	$13.827^{+0.179}_{-0.150}$	this work
3C273	4	0.0490	14691	$20^{+\infty}_{-9}$	$13.614^{+0.127}_{-0.083}$	this work
3C273	5	0.0665	19956	38^{+15}_{-10}	$13.978^{+0.051}_{-0.030}$	this work, [d]
3C273	6	0.0901	27036	$36^{+\infty}_{-17}$	$13.583^{+0.039}_{-0.131}$	this work
3C273	7	0.1201	36021	$28^{+\infty}_{-11}$	$13.534^{+0.047}_{-0.123}$	this work
3C273	8	0.1466	43980	$61^{+\infty}_{-19}$	$13.974^{+0.061}_{-0.057}$	this work
PG1259+593	1	0.0023	687	42 ± 4	$13.570^{+0.100}_{-0.100}$	Lyα fit, Richter et al (1994)
PG1259+593	2	0.0076	2280	33^{+10}_{-5}	$14.057^{+0.066}_{-0.070}$	this work
PG1259+593	3	0.0222	6651	17^{+15}_{-4}	$13.802^{+0.149}_{-0.169}$	this work
PG1259+593	5	0.0461	13818	30^{+10}_{-8}	$15.510^{+0.297}_{-0.253}$	this work
PG1259+593	6	0.0465	13950	37^{+20}_{-14}	$14.544^{+0.222}_{-0.126}$	this work
PG1259+593	7	0.0538	16127	$17^{+\infty}_{-9}$	$13.415^{+0.287}_{-0.147}$	this work
PG1259+593	8	0.0664	19932	18^{+14}_{-5}	$13.771^{+0.100}_{-0.124}$	this work
PG1259+593	9	0.0693	20793	88 ± 9	$13.140^{+0.090}_{-0.090}$	Lyα fit, Richter et al (1994)
PG1259+593	10	0.0893	26799	27 ± 4	$14.076^{+0.056}_{-0.052}$	this work
PG1259+593	11	0.1239	37165	12^{+12}_{-2}	$13.884^{+0.214}_{-0.303}$	this work
PG1259+593	12	0.1485	44556	32^{+18}_{-5}	$13.915^{+0.051}_{-0.086}$	this work
PG1259+593	13	0.1505	45150	32 ± 5	$13.450^{+0.130}_{-0.130}$	Lyα fit, Richter et al (1994)
PG1259+593	14	0.1962	58860	28^{+36}_{-6}	$13.784^{+0.025}_{-0.102}$	this work
PG1259+593	15	0.2195	65847	33 ± 3	$15.266^{+0.091}_{-0.036}$	this work
PG1259+593	16	0.2231	66939	26^{+6}_{-3}	$14.006^{+0.069}_{-0.076}$	this work
PG1259+593	17	0.2247	67413	27 ± 2	$13.665^{+0.026}_{-0.026}$	Lyα fit, this work
PG1259+593	18	0.2564	76926	28^{+33}_{-8}	$13.726^{+0.091}_{-0.108}$	this work
PG1259+593	19	0.2597	77913	30^{+13}_{-6}	$13.932^{+0.077}_{-0.077}$	this work
PG1259+593	20	0.2833	85005	34^{+42}_{-17}	$13.585^{+0.148}_{-0.099}$	this work
PG1259+593	21	0.2924	87708	32 ± 3	$14.501^{+0.058}_{-0.053}$	this work
PKS1302-102	1	0.0044	1311	18 ± 2	$14.872^{+0.286}_{-0.286}$	Lyα fit, this work
PKS1302-102	3	0.0423	12679	28 ± 2	$14.809^{+0.071}_{-0.088}$	this work
PKS1302-102	4	0.0445	13339	14^{+21}_{-3}	$13.846^{+0.194}_{-0.296}$	this work
PKS1302-102	5	0.0461	13839	47 ± 7	$13.376^{+0.050}_{-0.050}$	Lyα fit, this work
PKS1302-102	6	0.0466	13974	48 ± 3	$13.780^{+0.022}_{-0.022}$	Lyα fit, this work
PKS1302-102	7	0.0597	17902	25 ± 3	$13.291^{+0.047}_{-0.047}$	Lyα fit, this work
PKS1302-102	8	0.0647	19420	51^{+24}_{-20}	$13.789^{+0.107}_{-0.063}$	this work
PKS1302-102	9	0.0865	25965	9^{+3}_{-2}	$13.934^{+0.236}_{-0.217}$	this work
PKS1302-102	10	0.0940	28193	28^{+7}_{-2}	$14.832^{+0.106}_{-0.371}$	this work
PKS1302-102	21	0.0948	28450	59^{+17}_{-24}	$15.145^{+0.900}_{-0.245}$	this work
PKS1302-102	13	0.0989	29668	43^{+5}_{-4}	$14.491^{+0.076}_{-0.076}$	this work
PKS1302-102	14	0.1234	37009	9^{+7}_{-2}	$13.839^{+0.251}_{-0.310}$	this work
PKS1302-102	15	0.1453	43596	53 ± 7	$15.306^{+0.084}_{-0.079}$	this work
PKS1302-102	16	0.1916	57479	15^{+9}_{-6}	$15.461^{+0.821}_{-0.230}$	this work
PKS1302-102	17	0.2245	67362	38 ± 2	$14.043^{+0.035}_{-0.035}$	Lyα fit, this work
PKS1302-102	18	0.2255	67665	51 ± 2	$14.021^{+0.029}_{-0.013}$	Lyα fit, this work
PKS1302-102	19	0.2488	74630	12 ± 1	$14.911^{+0.275}_{-0.229}$	this work
PKS1302-102	20	0.2521	75633	44 ± 3	$14.351^{+0.055}_{-0.055}$	Lyα fit, this work

TABLE 3 — *Continued*

Target	Abs#	$z_{\rm abs}$	$cz_{\rm abs}$	$b_{\rm HI}$	$\log N_{\rm HI}$	notes[a]
Mrk1383	1	0.0283	8490	23^{+27}_{-8}	$13.933^{+0.141}_{-0.151}$	this work
Mrk1383	2	0.0519	15566	25^{+5}_{-4}	$14.200^{+0.086}_{-0.076}$	this work
Mrk817	1	0.0070	2097	$16^{+\infty}_{-8}$	$13.659^{+0.585}_{-0.280}$	this work
Mrk478	1	0.0053	1582	22^{+56}_{-6}	$13.839^{+0.025}_{-0.311}$	this work
Mrk478	2	0.0293	8788	27^{+29}_{-7}	$14.161^{+0.230}_{-0.240}$	this work
Mrk478	3	0.0653	19593	43 ± 6	$13.270^{+0.030}_{-0.010}$	Penton et al. (2004)
Mrk876	1	0.0032	958	24^{+12}_{-7}	$14.533^{+0.269}_{-0.274}$	this work
Mrk876	2	0.0116	3486	56 ± 10	$13.844^{+0.500}_{-0.500}$	Lyα fit, this work
H1821+643	1	0.0245	7342	25^{+7}_{-4}	$14.295^{+0.157}_{-0.146}$	this work
H1821+643	2	0.0569	17064	20 ± 10	$13.308^{+0.146}_{-0.040}$	$W_{\rm Ly\alpha}$ [b]
H1821+643	3	0.0672	20166	13^{+4}_{-3}	$14.045^{+0.183}_{-0.148}$	this work
H1821+643	4	0.1197	35903	8^{+2}_{-1}	$13.938^{+0.127}_{-0.131}$	this work
H1821+643	5	0.1213	36394	32^{+8}_{-6}	$14.406^{+0.090}_{-0.076}$	this work
H1821+643	6	0.1476	44274	> 33	$13.639^{+0.144}_{-0.014}$	this work
H1821+643	7	0.1699	50969	$59^{+\infty}_{-12}$	$14.277^{+0.104}_{-0.119}$	this work
H1821+643	10	0.2117	63510	8^{+4}_{-2}	$13.995^{+0.181}_{-0.311}$	this work
H1821+643	11	0.2131	63933	45^{+11}_{-6}	$14.378^{+0.093}_{-0.114}$	this work
H1821+643	12	0.2160	64803	$11^{+\infty}_{-1}$	$14.075^{+0.019}_{-0.654}$	this work
H1821+643	13	0.2247	67420	24^{+3}_{-2}	$15.239^{+0.180}_{-0.134}$	this work, [b]
H1821+643	14	0.2261	67836	$26^{+\infty}_{-3}$	$14.148^{+0.000}_{-0.388}$	this work
H1821+643	15	0.2264	67911	20 ± 10	$13.568^{+0.034}_{-0.037}$	Tripp et al. (2000)
H1821+643	19	0.2584	77507	20 ± 10	$13.465^{+0.258}_{-0.057}$	$W_{\rm Ly\alpha}$ [b]
H1821+643	20	0.2613	78398	20 ± 10	$13.820^{+0.980}_{-0.133}$	$W_{\rm Ly\alpha}$ [b]
H1821+643	21	0.2666	79977	20 ± 10	$13.623^{+0.030}_{-0.032}$	Tripp et al. (2000)
PKS2005-489	1	0.0165	4947	$38^{+\infty}_{-12}$	$13.981^{+0.143}_{-0.127}$	this work
PKS2005-489	2	0.0169	5061	18^{+3}_{-4}	$14.782^{+0.667}_{-0.202}$	this work
PKS2005-489	3	0.0577	17306	$32^{+\infty}_{-9}$	$14.055^{+0.211}_{-0.251}$	this work
PKS2005-489	4	0.0649	19478	23^{+6}_{-4}	$14.113^{+0.120}_{-0.114}$	this work
Mrk509	1	0.0085	2560	22^{+34}_{-8}	$13.914^{+0.161}_{-0.162}$	this work
IIZw136	1	0.0277	8320	13^{+5}_{-4}	$14.402^{+0.568}_{-0.287}$	this work
PHL1811	1	0.0118	3537	45 ± 9	$14.060^{+0.500}_{-0.500}$	Lyα fit, this work
PHL1811	2	0.0173	5201	24 ± 5	$13.990^{+0.500}_{-0.500}$	Lyα fit, this work
PHL1811	3	0.0501	15017	9^{+2}_{-1}	$14.141^{+0.146}_{-0.195}$	this work
PHL1811	4	0.0514	15426	20^{+8}_{-3}	$14.237^{+0.180}_{-0.240}$	this work
PHL1811	5	0.0734	22020	27 ± 8	$15.120^{+0.230}_{-0.050}$	this work
PHL1811	6	0.0777	23311	26 ± 6	$14.890^{+0.500}_{-0.500}$	Lyα fit, this work
PHL1811	7	0.0790	23688	24 ± 8	$15.940^{+0.500}_{-0.500}$	Lyα fit, this work
PHL1811	8	0.0807	24215	12^{+4}_{-2}	$18.112^{+0.117}_{-0.182}$	this work
PHL1811	9	0.1322	39664	32 ± 6	$14.628^{+0.164}_{-0.055}$	this work
PHL1811	10	0.1354	40606	18 ± 3	$14.684^{+0.186}_{-0.048}$	this work
PHL1811	11	0.1764	52919	29 ± 7	$14.952^{+0.173}_{-0.102}$	this work
PHL1811	12	0.1808	54251	26 ± 8	$13.240^{+0.500}_{-0.500}$	Lyα fit, this work
PKS2155-304	1	0.0167	5013	$14^{+\infty}_{-9}$	$13.339^{+0.180}_{-0.155}$	this work
PKS2155-304	2	0.0171	5119	16 ± 4	$14.409^{+0.372}_{-0.184}$	this work, [d]
PKS2155-304	3	0.0453	13591	$29^{+\infty}_{-21}$	$13.353^{+0.174}_{-0.146}$	this work
PKS2155-304	4	0.0540	16185	38^{+9}_{-5}	$14.071^{+0.046}_{-0.055}$	this work, [d]
PKS2155-304	5	0.0566	16974	40^{+17}_{-6}	$14.548^{+0.196}_{-0.283}$	this work
PKS2155-304	6	0.0572	17147	87 ± 11	$14.100^{+0.500}_{-0.500}$	Penton et al. (2000, 2002)
PKS2155-304	7	0.0590	17713	13^{+30}_{-4}	$13.847^{+0.309}_{-0.286}$	this work
PKS2155-304	8	0.0602	18073	8^{+6}_{-3}	$13.910^{+0.416}_{-0.293}$	this work
MR2251-178	1	0.0107	3205	69 ± 4	$14.610^{+1.000}_{-0.290}$	Penton et al. (2004)
MR2251-178	2	0.0325	9735	$18^{+\infty}_{-6}$	$13.876^{+0.256}_{-0.277}$	this work

[a] Unless otherwise noted, quoted $b_{\rm HI}$ and $\log N_{\rm HI}$ values are based on concordance plots using multiple Lyman lines. "Lyα fit" denotes cases based on Voigt fits to Lyα only.

[b] Column density estimate based on $W_{\rm Ly\alpha}$ and assumed $b = 20 \pm 10$ km s^{-1}.

[c] Deviation of $> 2\sigma$ in $b_{\rm HI}$ compared with published, this work-qualified measurement.

[d] Deviation of $> 2\sigma$ in $N_{\rm HI}$ compared with published, this work-qualified measurement.

TABLE 4
O VI Absorber Detections and Upper Limits

Sight Line	Abs #	$z_{\rm abs}$	$cz_{\rm abs}$ (km s^{-1})	b_{1032} (km s^{-1})	W_{1032} (mÅ)	b_{1032} (km s^{-1})	W_{1038} (mÅ)	log N(OVI)	notes
Mrk335	1	0.0066	1965	···	···	···	< 10	< 13.21	
Mrk335	2	0.0077	2295	···	< 9	···	< 10	< 12.87	
Mrk335	3	0.0209	6269	···	< 31	···	< 17	< 13.42	
IZw1	2	0.0095	2861	···	< 42	···	< 39	< 13.57	
TonS180	1	0.0183	5502	···	< 20	···	< 20	< 13.22	
TonS180	2	0.0234	7017	30	43 ± 15	···	< 20	13.48 ± 0.05	
TonS180	3	0.0430	12912	···	< 17	···	< 18	< 13.15	
TonS180	4	0.0436	13068	40	31 ± 18	···	···	13.43 ± 0.02	
TonS180	5	0.0450	13515	···	< 17	···	< 66	< 13.15	
TonS180	6	0.0456	13681	20	62 ± 14	34	78 ± 60	13.74 ± 0.06	$\Delta v \sim +70$ km s^{-1}
HE0226-4110	1	0.0294	8815	···	···	···	< 32	< 13.74	
HE0226-4110	2	0.0461	13817	···	< 39	···	···	< 13.81	
PKS0405-123	1	0.0300	8989	···	···	···	< 105	< 14.35	blend
PKS0405-123	3	0.0918	27549	21	49 ± 11	···	< 24	13.58 ± 0.05	
PKS0405-123	4	0.0966	28970	39	73 ± 12	17	28 ± 9	13.70 ± 0.06	
PKS0405-123	7	0.1310	39285	···	< 16	···	< 24	< 13.12	
PKS0405-123	8	0.1323	39683	···	···	···	< 17	< 13.45	
Akn120	1	0.0265	7960	···	< 28	···	···	< 13.38	
VIIZw118	1	0.0082	2460	···	···	···	< 18	< 13.48	
PG0804+761	1	0.0038	1147	17	36 ± 10	···	···	13.52 ± 0.12	edge of Galactic CII
PG0804+761	2	0.0185	5552	···	···	···	< 9	< 13.17	
PG0953+415	1	0.0160	4806	···	< 23	···	< 19	< 13.27	
PG0953+415	2	0.0166	4965	···	< 16	···	< 14	< 13.12	
PG0953+415	3	0.0588	17628	35	47 ± 10	48	29 ± 12	13.58 ± 0.11	
PG0953+415	4	0.0681	20421	16	108 ± 8	14	82 ± 8	14.15 ± 0.07	
PG0953+415	5	0.0931	27945	···	< 11	···	···	< 12.96	
PG0953+415	6	0.1094	32817	···	···	···	< 23	< 13.61	
PG0953+415	7	0.1156	34674	···	< 16	···	< 30	< 13.12	
PG0953+415	8	0.1183	35478	···	< 23	···	< 17	< 13.30	
PG0953+415	9	0.1280	38403	···	< 13	···	< 13	< 13.03	
PG0953+415	18	0.1425	42739	20	100 ± 10	32	96 ± 17	14.05 ± 0.10	
PG0953+415	19	0.1426	42774	53	133 ± 18	46	98 ± 23	14.22 ± 0.06	
Mrk421	1	0.0101	3035	···	< 9	···	···	< 12.87	
PG1116+215	1	0.0050	1499	···	···	21	45 ± 11	13.91 ± 0.10	
PG1116+215	2	0.0164	4913	···	< 14	···	< 184	< 13.06	
PG1116+215	4	0.0284	8518	···	< 11	···	< 10	< 12.96	
PG1116+215	5	0.0323	9705	···	< 11	···	< 10	< 12.96	
PG1116+215	6	0.0412	12357	···	< 26	···	< 12	< 13.29	
PG1116+215	7	0.0590	17698	24	38 ± 6	24	35 ± 7	13.58 ± 0.13	$\Delta v \sim +50$ km s^{-1}
PG1116+215	8	0.0812	24369	26	< 11	···	···	< 13.01	
PG1116+215	9	0.1191	35735	···	< 12	···	< 11	< 12.99	
PG1116+215	10	0.1386	41579	25	57 ± 9	10	23 ± 7	13.60 ± 0.05	
PG1211+143	1	0.0071	2130	···	···	50	45 ± 14	13.90 ± 0.02	
PG1211+143	2	0.0165	4944	···	< 23	···	< 13	< 13.31	
PG1211+143	3	0.0168	5036	···	···	···	< 13	< 13.33	
PG1211+143	4	0.0221	6615	···	< 13	···	< 14	< 13.03	
PG1211+143	5	0.0233	7002	···	< 28	···	< 19	< 13.35	
PG1211+143	6	0.0258	7752	···	< 15	···	···	< 13.09	
PG1211+143	7	0.0434	13010	···	< 15	···	···	< 13.09	
PG1211+143	8	0.0436	13068	···	< 22	···	···	< 13.30	
PG1211+143	14	0.0513	15384	···	···	60	122 ± 13	14.30 ± 0.02	two HI components
PG1211+143	11	0.0520	15605	···	< 41	···	···	< 13.56	
PG1211+143	12	0.0644	19328	40	126 ± 16	58	73 ± 12	14.10 ± 0.04	
PG1211+143	13	0.0649	19468	21	43 ± 11	49	49 ± 12	13.91 ± 0.20	
3C273	1	0.0034	1015	47	35 ± 6	···	···	13.46 ± 0.07	
3C273	2	0.0053	1586	···	···	···	< 9	< 13.17	
3C273	3	0.0294	8832	···	< 8	···	< 9	< 12.81	
3C273	4	0.0490	14691	···	< 15	···	< 11	< 13.09	
3C273	5	0.0665	19956	···	< 7	···	< 13	< 12.81	
3C273	6	0.0901	27036	24	13 ± 6	20	13 ± 3	13.05 ± 0.11	
3C273	7	0.1201	36021	15	24 ± 3	15	15 ± 4	13.23 ± 0.04	
3C273	8	0.1466	43980	···	< 9	···	···	< 12.87	
PG1259+593	1	0.0023	687	17	14 ± 9	···	···	13.07 ± 0.09	
PG1259+593	2	0.0076	2280	···	···	···	< 15	< 13.39	
PG1259+593	3	0.0222	6651	16	< 34	···	< 10	< 13.21	
PG1259+593	5	0.0461	13818	40	95 ± 15	···	···	13.91 ± 0.04	
PG1259+593	6	0.0465	13950	21	60 ± 12	···	···	13.72 ± 0.06	
PG1259+593	7	0.0538	16127	72	< 40	58	< 21	< 13.54	edge of LiF1a detector
PG1259+593	8	0.0664	19932	6	< 10	···	< 8	< 12.91	
PG1259+593	9	0.0693	20793	···	< 9	···	< 8	< 12.87	
PG1259+593	10	0.0893	26799	···	< 9	···	< 9	< 12.89	
PG1259+593	11	0.1239	37165	···	< 9	···	< 9	< 12.87	
PG1259+593	12	0.1485	44556	···	< 15	···	···	< 13.09	
PG1259+593	13	0.1505	45150	46	45 ± 14	···	···	13.46 ± 0.07	

TABLE 4 — *Continued*

Sight Line	Abs #	$z_{\rm abs}$	$cz_{\rm abs}$ (km s^{-1})	b_{1032} (km s^{-1})	W_{1032} (mÅ)	b_{1032} (km s^{-1})	W_{1038} (mÅ)	log N(OVI)	notes
PKS1302-102	3	0.0423	12679	56	232 ± 19	···	···	14.36 ± 0.02	multiple components?
PKS1302-102	4	0.0445	13339	···	< 20	···	···	< 13.27	
PKS1302-102	5	0.0461	13839	···	< 26	···	···	< 13.38	
PKS1302-102	6	0.0466	13974	···	< 33	···	···	< 13.48	
PKS1302-102	7	0.0597	17902	···	< 20	···	< 16	< 13.22	
PKS1302-102	8	0.0647	19420	35	60 ± 14	46	< 35	13.67 ± 0.07	
PKS1302-102	9	0.0865	25965	···	< 17	···	···	< 13.15	
PKS1302-102	10	0.0940	28193	9	19 ± 10	···	···	13.15 ± 0.14	
PKS1302-102	21	0.0948	28450	63	84 ± 18	44	30 ± 17	13.75 ± 0.12	two HI absorbers
PKS1302-102	13	0.0989	29668	···	···	52	68 ± 19	13.99 ± 0.08	
PKS1302-102	14	0.1234	37009	···	< 20	···	< 23	< 13.22	
PKS1302-102	15	0.1453	43596	93	146 ± 35	···	···	14.16 ± 0.03	broad, multiple?
Mrk1383	1	0.0283	8490	···	< 16	···	< 18	< 13.10	
Mrk1383	2	0.0519	15566	21	66 ± 25	27	21 ± 8	13.83 ± 0.19	$\Delta v \sim -60$ km s^{-1}
Mrk817	1	0.0070	2097	···	···	···	< 6	< 12.99	
Mrk478	1	0.0053	1582	···	···	···	< 67	< 14.16	
Mrk478	2	0.0293	8788	···	···	···	< 29	< 13.69	
Mrk876	1	0.0032	958	13	26 ± 7	···	···	13.37 ± 0.10	H_2 blend removed
Mrk876	2	0.0116	3486	···	< 16	···	···	< 13.12	
H1821+643	1	0.0245	7342	23	32 ± 16	···	···	13.43 ± 0.17	broad line, multiple?
H1821+643	2	0.0569	17064	···	< 25	···	< 74	< 13.34	
H1821+643	3	0.0672	20166	···	< 14	···	< 46	< 13.06	
H1821+643	4	0.1197	35903	···	< 12	···	< 14	< 12.99	
H1821+643	5	0.1213	36394	45	53 ± 25	27	134 ± 18	13.56 ± 0.12	
H1821+643	6	0.1476	44274	···	< 20	···	···	< 13.22	
PKS2005-489	1	0.0165	4947	···	< 15	···	< 14	< 13.09	
PKS2005-489	2	0.0169	5061	···	< 59	···	< 125	< 13.74	
PKS2005-489	3	0.0577	17306	···	< 16	···	< 16	< 13.12	
PKS2005-489	4	0.0649	19478	28	62 ± 13	36	19 ± 18	13.61 ± 0.07	multiple components?
Mrk509	1	0.0085	2560	···	< 19	···	< 13	< 13.20	
PHL1811	1	0.0118	3537	20	< 63	···	···	< 13.78	
PHL1811	2	0.0173	5201	···	< 350	17	44 ± 9	13.90 ± 0.07	possible blend
PHL1811	3	0.0501	15017	···	< 68	···	< 70	< 13.91	
PHL1811	4	0.0514	15426	···	< 47	···	< 58	< 13.62	
PHL1811	5	0.0734	22020	···	< 14	···	< 14	< 13.06	
PHL1811	6	0.0777	23311	···	< 55	···	< 15	< 13.39	
PHL1811	7	0.0790	23688	···	< 14	···	< 15	< 13.06	
PHL1811	8	0.0807	24215	···	< 14	···	< 15	< 13.06	Lyman limit system
PHL1811	9	0.1322	39664	···	···	33	53 ± 17	13.86 ± 0.08	
PHL1811	10	0.1354	40606	···	< 75	···	< 26	< 13.74	
PKS2155-304	1	0.0167	5013	50	< 15	···	< 6	< 12.99	
PKS2155-304	2	0.0171	5119	···	< 8	···	< 34	< 12.84	
PKS2155-304	3	0.0453	13591	···	< 7	···	···	< 12.76	
PKS2155-304	4	0.0540	16185	27	40 ± 5	17	32 ± 5	13.61 ± 0.11	$\Delta v \sim +74$ km s^{-1}
PKS2155-304	5	0.0566	16974	···	< 32	···	< 7	< 13.06	
PKS2155-304	6	0.0572	17147	30	55 ± 6	···	< 96	13.65 ± 0.02	
PKS2155-304	7	0.0590	17713	···	< 18	···	< 7	< 13.06	broad line
PKS2155-304	8	0.0602	18073	···	< 9	···	< 7	< 12.87	
MR2251-178	1	0.0107	3205	14	29 ± 16	···	< 24	13.42 ± 0.20	
MR2251-178	2	0.0325	9735	···	< 26	···	< 39	< 13.35	

TABLE 5
C III Absorber Detections and Upper Limits

Sight Line	Abs #	$z_{\rm abs}$	$cz_{\rm abs}$ (km s^{-1})	b_{977} (km s^{-1})	W_{977} (mÅ)	log N(CIII)	notes
Mrk335	2	0.0077	2295	13	25 ± 13	12.63 ± 0.19	
Mrk335	3	0.0209	6269	···	< 18	< 12.47	
IZw1	3	0.0171	5130	···	< 701	< 13.92	
TonS180	2	0.0234	7017	···	< 30	< 12.70	
TonS180	3	0.0430	12912	···	< 21	< 12.52	
TonS180	4	0.0436	13068	···	< 48	< 12.95	
TonS180	5	0.0450	13515	···	< 21	< 12.52	
TonS180	6	0.0456	13681	13	48 ± 12	12.95 ± 0.07	
HE0226-4110	1	0.0294	8815	···	< 45	< 13.07	
HE0226-4110	2	0.0461	13817	···	< 27	< 12.64	
HE0226-4110	4	0.1633	48983	···	< 24	< 12.60	
HE0226-4110	5	0.1938	58134	···	< 27	< 12.67	
HE0226-4110	6	0.1985	59537	···	< 77	< 13.01	
HE0226-4110	7	0.2069	62064	27	237 ± 38	13.83 ± 0.02	
PKS0405-123	4	0.0966	28970	···	< 167	< 13.50	blend
PKS0405-123	7	0.1310	39285	···	< 14	< 12.35	
PKS0405-123	8	0.1323	39683	···	< 14	< 12.35	
PKS0405-123	9	0.1670	50109	···	< 363	< 14.24	
PKS0405-123	10	0.1827	54809	34	210 ± 26	13.65 ± 0.03	two components[a]
Akn120	1	0.0265	7960	···	< 80	< 13.27	
VIIZw118	1	0.0082	2460	···	< 37	< 12.79	
PG0804+761	1	0.0038	1147	···	< 82	< 13.21	
PG0804+761	2	0.0185	5552	···	< 148	< 13.59	
PG0953+415	1	0.0160	4806	···	< 92	< 13.47	
PG0953+415	2	0.0166	4965	···	< 32	< 12.89	
PG0953+415	3	0.0588	17628	···	< 16	< 12.42	
PG0953+415	4	0.0681	20421	20	77 ± 10	13.15 ± 0.02	
PG0953+415	5	0.0931	27945	···	< 13	< 12.35	
PG0953+415	6	0.1094	32817	···	< 486	< 14.19	
PG0953+415	7	0.1156	34674	···	< 18	< 12.52	
PG0953+415	8	0.1183	35478	···	< 43	< 12.76	
PG0953+415	11	0.1798	53952	···	< 65	< 12.92	
PG0953+415	12	0.1914	57426	···	< 13	< 12.35	
PG0953+415	13	0.1922	57663	···	< 13	< 12.35	
PG0953+415	14	0.1936	58080	···	< 13	< 12.35	
PG0953+415	18	0.1425	42739	46	44 ± 11	12.75 ± 0.05	
PG0953+415	19	0.1426	42774	76	61 ± 14	13.08 ± 0.01	
Mrk421	1	0.0101	3035	36	< 79	< 13.14	
PG1116+215	1	0.0050	1499	···	< 56	< 13.01	
PG1116+215	2	0.0164	4913	···	< 20	< 12.52	
PG1116+215	4	0.0284	8518	···	< 14	< 12.35	
PG1116+215	5	0.0323	9705	15	37 ± 7	12.81 ± 0.06	H_2 deblended
PG1116+215	6	0.0412	12357	···	< 16	< 12.42	
PG1116+215	7	0.0590	17698	···	< 22	< 12.59	
PG1116+215	8	0.0812	24369	···	< 46	< 12.82	
PG1116+215	9	0.1191	35735	5	27 ± 9	12.71 ± 0.04	$\Delta v \sim -70$ km s^{-1}
PG1116+215	10	0.1386	41579	16	116 ± 6	13.46 ± 0.03	
PG1116+215	11	0.1663	49876	26	66 ± 6	12.95 ± 0.03	
PG1116+215	12	0.1737	52104	43	71 ± 11	13.08 ± 0.02	two components[a]
PG1211+143	1	0.0071	2130	···	< 66	< 13.09	
PG1211+143	2	0.0165	4944	···	< 73	< 13.21	
PG1211+143	5	0.0233	7002	···	< 22	< 12.56	
PG1211+143	7	0.0434	13010	···	< 14	< 12.35	
PG1211+143	8	0.0436	13068	···	< 14	< 12.35	
PG1211+143	14	0.0513	15384	23	222 ± 35	13.88 ± 0.05	two components[a]
PG1211+143	11	0.0520	15605	···	< 13	< 12.35	
PG1211+143	12	0.0644	19328	35	169 ± 11	13.53 ± 0.03	
PG1211+143	13	0.0649	19468	···	< 73	< 13.16	
3C273	1	0.0034	1015	···	< 22	< 12.61	
3C273	3	0.0294	8832	···	< 8	< 12.20	
3C273	5	0.0665	19956	···	< 9	< 12.20	
3C273	7	0.1201	36021	···	< 7	< 12.20	
3C273	8	0.1466	43980	···	< 6	< 12.20	
PG1259+593	1	0.0023	687	···	< 15	< 12.35	
PG1259+593	2	0.0076	2280	···	< 18	< 12.47	
PG1259+593	3	0.0222	6651	···	< 42	< 12.89	
PG1259+593	5	0.0461	13818	30	216 ± 10	13.79 ± 0.00	
PG1259+593	6	0.0465	13950	20	110 ± 7	13.40 ± 0.01	
PG1259+593	7	0.0538	16127	···	< 9	< 12.20	
PG1259+593	10	0.0893	26799	···	< 11	< 12.29	
PG1259+593	12	0.1485	44556	···	< 49	< 12.94	
PG1259+593	13	0.1505	45150	···	< 9	< 12.20	
PKS1302-102	1	0.0044	1311	···	< 66	< 13.24	
PKS1302-102	3	0.0423	12679	27	116 ± 22	13.36 ± 0.05	IGM blend removed

TABLE 5 — *Continued*

Sight Line	Abs #	$z_{\rm abs}$	$cz_{\rm abs}$ (km s^{-1})	b_{977} (km s^{-1})	W_{977} (mÅ)	log N(CIII)	notes
PKS1302-102	4	0.0445	13339	17	22 ± 10	12.53 ± 0.16	
PKS1302-102	5	0.0461	13839	···	< 15	< 12.35	
PKS1302-102	6	0.0466	13974	···	< 15	< 12.35	
PKS1302-102	7	0.0597	17902	···	< 18	< 12.50	
PKS1302-102	8	0.0647	19420	···	< 25	< 12.68	
PKS1302-102	9	0.0865	25965	23	16 ± 17	12.45 ± 0.12	$\Delta v \sim +40$ km s^{-1}
PKS1302-102	10	0.0940	28193	···	< 282	< 13.81	IGM blend
PKS1302-102	21	0.0948	28450	45	258 ± 50	13.73 ± 0.05	two components[a]
PKS1302-102	13	0.0989	29668	···	< 70	< 12.99	IGM blend
PKS1302-102	14	0.1234	37009	···	< 18	< 12.47	
PKS1302-102	15	0.1453	43596	78	73 ± 20	13.00 ± 0.05	two components[a]
PKS1302-102	16	0.1916	57479	11	38 ± 12	12.74 ± 0.04	
Mrk1383	1	0.0283	8490	···	< 17	< 12.50	
Mrk817	1	0.0070	2097	···	< 13	< 12.29	
Mrk478	1	0.0053	1582	···	< 247	< 13.92	
Mrk478	2	0.0293	8788	10	42 ± 27	12.93 ± 0.18	
Mrk876	1	0.0032	958	···	< 29	< 12.70	
H1821+643	1	0.0245	7342	···	< 26	< 12.64	
H1821+643	2	0.0569	17064	···	< 22	< 12.62	
H1821+643	3	0.0672	20166	···	< 13	< 12.35	
H1821+643	5	0.1213	36394	···	< 12	< 12.29	
H1821+643	6	0.1476	44274	···	< 12	< 12.29	
H1821+643	7	0.1699	50969	22	43 ± 11	12.74 ± 0.04	FeII blend removed
H1821+643	10	0.2117	63510	···	< 18	< 12.47	
H1821+643	11	0.2131	63933	···	< 18	< 12.47	
PKS2005-489	1	0.0165	4947	···	< 36	< 12.79	
PKS2005-489	2	0.0169	5061	42	152 ± 26	13.48 ± 0.06	H_2 blend removed
PKS2005-489	3	0.0577	17306	···	< 15	< 12.35	
PKS2005-489	4	0.0649	19478	···	< 14	< 12.35	
PHL1811	5	0.0734	22020	···	< 216	< 13.63	IGM blend
PHL1811	6	0.0777	23311	26	149 ± 9	13.52 ± 0.01	multiple components?
PHL1811	7	0.0790	23688	···	< 15	< 12.35	
PHL1811	8	0.0807	24215	46	291 ± 32	13.98 ± 0.05	multiple components[a,b]
PHL1811	9	0.1322	39664	17	26 ± 8	12.54 ± 0.07	
PHL1811	10	0.1354	40606	12	58 ± 8	13.01 ± 0.00	
PHL1811	11	0.1764	52919	58	194 ± 30	13.72 ± 0.04	two components[a]
PHL1811	12	0.1808	54251	···	< 20	< 12.52	
PKS2155-304	1	0.0167	5013	···	< 18	< 12.45	
PKS2155-304	2	0.0171	5119	···	< 13	< 12.29	
PKS2155-304	3	0.0453	13591	···	< 6	< 12.20	
PKS2155-304	4	0.0540	16185	···	< 10	< 12.20	
PKS2155-304	6	0.0572	17147	···	< 9	< 12.20	
PKS2155-304	7	0.0590	17713	···	< 6	< 12.20	
PKS2155-304	8	0.0602	18073	···	< 50	< 12.93	HVC blend

[a] Absorber shows clear multiple structure. Quoted values are sums of individually fit components.
[b] Strong absorber associated with Lyman limit system.